Howe, T., Christopher, T., Moune, S., Tuffen, H., Cole, P. and Schiavi, F. (2026) “Volatile emissions and magma storage conditions for the 2021 explosive eruption at La Soufrière volcano, St Vincent from melt inclusions”, Volcanica, 9(1). doi: 10.30909/vol/odlf5080.

Volatile emissions and magma storage conditions for the 2021 explosive eruption at La Soufrière volcano, St Vincent from melt inclusions

TiVonne A. Howe*[1], Thomas E. Christopher[2,3], Séverine Moune[4,5], Hugh Tuffen[1], Paul D. Cole[6], Federica Schiavi[4]

[1] Lancaster Environment Centre, Lancaster University, Lancaster, United Kingdom
[2] Montserrat Volcano Observatory, Flemmings, Montserrat
[3] Seismic Research Centre, The University of the West Indies, St Augustine, Trinidad and Tobago
[4] Laboratoire Magmas et Volcans, Observatoire de Physique du Globe de Clermont-Ferrand, Université Clermont Auvergne, Clermont-Ferrand, France
[5] Université Paris Cité, Institut de Physique du Globe de Paris, Paris, France
[6] School of Geography, Earth and Environmental Sciences, University of Plymouth, Plymouth, UK

* tivonnehowe@live.com [corresponding author]
ORCiD (TAH): 0009.0005.9385.544X
ORCiD (TEC): 0000.0002.5968.5070
ORCiD (SM): 0000.0002.8485.0154
ORCiD (HT): 0000.0001.8829.1751
ORCiD (PC): 0000.0002.2964.311X
ORCiD (FS): 0000.0001.9801.1581

Keywords: Vapour Bubble; Melt Inclusion; Magma Degassing; Volatile Emissions; Volatile Budget; Lesser Antilles

Abstract

The VEI 4 eruption of La Soufrière volcano underwent a dramatic transition in style from initial lava dome effusion in December 2020 to hazardous explosive activity in April 2021. Understanding the magmatic processes underpinning such transitions is critical. We provide the first comprehensive dataset of the compositions and volatile contents of melt inclusions from the 2021 explosive activity, including the first measurements of pre-eruptive total CO_2 at La Soufrière and estimates of magmatic

temperature. We use the petrological method to quantify volatile fluxes to the atmosphere of 5.40±0.60 Mt H_2O, 0.37±0.04 Mt CO_2, 0.13±0.01 Mt SO_2, and 0.33±0.04 Mt HCl. Modelling of volatile saturation pressures indicates final magma storage depths of 2.4-8.9 km (mean 6.4 km) throughout four phases of explosive activity after migration of magma in the lower storage region within the transcrustal mush system. Inferred depths are consistent with recorded seismicity and deformation before and during the explosions.

Introduction

Volatiles are a key component of magmatic systems, influencing magma storage, ascent, eruptive mechanisms and the characteristics of volcanic eruptions at the surface (e.g. Cashman and Scheu, 2015). They are also important due to their environmental effects, including climate perturbations and the atmospheric impact of gas and aerosol emissions (e.g. Young et al., 1994; Robock, 2000; Hegerl et al., 2003; Schurer et al., 2014). Volatiles are exsolved from ascending magmas upon reaching vapour saturation, which can be influenced by pressure, temperature, composition, crystallisation and the solubility of specific volatile species in magmas. The explosive-effusive nature of eruptive activity e.g. Cassidy et al., 2018), can be influenced by volatiles, with retention of magmatic volatiles favouring violent acceleration and fragmentation of ascending magma, and thus explosive events, whereas in

situations where gases can exsolve and physically separate from the magma, effusive activity is mostly favoured (Cashman and Mangan, 1994; Johnson et al., 1994; Roggensack et al., 1997; Edmonds and Wallace, 2017; Edmonds and Woods, 2018).

While large eruptions often release significant amounts of volatiles into the atmosphere, ground based measurements of these volatile emissions are often sparse, or unachievable during eruptions, and are supplemented by other techniques such as satellite measurements (e.g. Theys et al., 2019; Queißer et al., 2019; Burton et al., 2021; Cofano et al., 2021). Additionally, quantification of emitted magmatic volatiles can be complicated by the scrubbing effect of hydrothermal systems, where emissions of certain volatile species may be reduced by interactions between magmatic gas and water or rock (e.g. dissolution of SO_2 into water; Symonds et al., 2001) or be lost to the atmosphere. Within this context, there is much value in petrological methods for determining overall volatile budgets of eruptions, which can provide a minimum estimate of the amount of volatiles released by comparing the pre-eruptive volatile concentrations of magma as recorded by the melt (Moore and Bodnar, 2019) with those of erupted material, taking into account the emitted volume of magma (Devine et al., 1984). The difference indicates the amount of gas released to the environment (both at the surface and subsurface of the Earth).

La Soufrière Volcano (Lindsay et al., 2005; Cole et al., 2019; Robertson et al., 2023) has been one of the most historically active subaerial volcanoes in the Lesser Antilles arc (Wadge, 1984) and is known for having both effusive and explosive styles. Like many arc volcanoes capable of producing large explosive eruptions, a considerable population exists in close proximity to the volcano and improved constraints on volatile systematics underpins improved hazard management. Volatile systematic constraints also advances our understanding of global volatile cycles, including carbon exchange between the inner Earth and the atmosphere. The volcanic hazards at St Vincent were recently emphasised in the 2020-2021 eruptions, which involved roughly three months of crater contained lava effusion followed by an abrupt transition to explosive activity on April 9th 2021 (Joseph et al., 2022; Camejo-Harry et al., 2023; Latchman and Aspinall, 2023; Robertson et al., 2023)

A key challenge at St Vincent and at other arc volcanoes worldwide is to understand the physicochemical processes underpinning the transitions in eruptive styles, similar to what occurred in the 2020-21 La Soufrière eruption, and specifically how they relate to the plumbing system of the volcano and the nature of its unrest. Previous estimates on magma storage pressures and corresponding depths at La Soufrière have been estimated using mineral thermobarometry and experimental petrology (e.g. Melekhova et al., 2015; Fedele et al., 2021; Weber et al., 2023), and whilst valuable, some petrological techniques involve significant uncertainties (Wieser et al., 2023). However, parcels of melt trapped in crystallising minerals (melt inclusions) can be used to infer the composition of the magma at the time of entrapment/crystallisation and can be used to provide additional constraints on magmatic

conditions such as pressure and depth if any subsequent changes during ascent are accounted for, and together with groundmass glass, calculate volatile mass released during eruptions.

In this study, we quantify the concentration of major and volatile elements (H_2O, S, Cl and F) in pyroclasts emitted in the April 2021 explosive activity and provide the first measurements of total magmatic CO_2 at La Soufrière volcano. The chemical composition of magma trapped as melt inclusions found in the olivine, plagioclase, orthopyroxene and clinopyroxene phenocrysts of the 2021 explosive activity allows for the reconstruction of magma storage conditions, magma evolution, La Soufrière's pre-eruptive budget, and an estimation of volatile loading into the atmosphere.

Geological Setting and History of La Soufrière Volcano

Geological Setting

The Lesser Antilles Arc is the surface manifestation of subduction of an oceanic portion of the western Atlantic Plate (North and South American Plates) beneath the eastern boundary of the Caribbean plate, forming an island arc subduction zone (Macdonald et al., 2000; Evian et al., 2013; Melekhova et al., 2019).

The arc is approximately 850 km long and is aligned submeridionally (Christeson et al., 2008; Evian et al., 2013; Kopp et al., 2011). Geophysical data suggests a convergence rate of ~2cm /year in a 67° ENE trend (DeMets, et al., 2000), leading to relatively low magma production rates (Macdonald et al., 2000), which inexorably leads to a lower tempo of eruptions along the arc.

La Soufrière Volcano

St Vincent is located in the southern section of the Lesser Antilles arc and is made up of Pliocene to recent lava and pyroclasts of basalt and basaltic andesite composition (Aspinall et al., 1973) which are the products of four stratovolcanoes (Le Friant et al., 2009, Cole et al., 2019). All are extinct except La Soufrière volcano. Based on K-Ar dating, the major centres show progression from south to north over time, with the earliest construction of La Soufrière beginning during the late Pleistocene, around 700

ka (Briden et al., 1979). Presently, La Soufrière Volcano (Figure 1) is a 1220 m high stratovolcano whose base extends outwards to 11km (Aspinall et al., 1973; Shepherd et al., 1979) and is one of the twenty-one potentially active volcanoes in the Lesser Antilles Arc (Lindsay et al., 2005).

Over the last 600 years, La Soufrière has experienced at least 7 explosive eruptions, along with 6 effusive eruptions (Shepard et al., 1979; Cole et al., 2019). Eruptions at La Soufrière have been (i) effusive only, generally associated with no pre- or syn-eruptive seismicity, lower magma effusion rate and lower volume of erupted material, producing lava domes, (ii) explosive only, associated with high explosivity, strong earthquakes, high magma production rate and large volumes of ejecta, or (iii) transitional eruptions where the eruption style changes from effusive to explosive or vice versa (Aspinall et al., 1973; Lindsay et al., 2005; Le Friant et al., 2009). At La Soufrière, there have only been two recorded instances of transitional eruptions – the explosive to effusive eruption of 1979 and the effusive to explosive 2020–2021 eruption. Over the 600-year period, the repose period between explosive events has spanned 140 and 77 years, and decreased with each event (Cole et al., 2019). The repose period between the two most recent eruptions in 1979 and 2020-2021 is 41 years, a continuation of this shortening trend of repose periods between eruptions observed at the La Soufrière volcano.

27th December 2020 – 22nd April 2021 Eruption

The 2020-2021 eruption of La Soufrière is extensively described in Joseph et al., (2022) and Robertson et al., (2023); however, a brief overview is provided here for context.

Pre-Explosive Activity

On 27th December 2020, satellite observations noted a hotspot in the La Soufrière crater, as a new dome began to grow adjacent to the 1979 dome (Joseph et al., 2022). The formation of the dome spanned 103 days, emplacing 16-19 million m^3 (Dualeh et al., 2023; Stinton et al., 2023) of basaltic andesite (Joseph et al., 2023). Notably, the first 13 days of dome emplacement were aseismic, suggesting unobstructed flow of degassed magma to the surface (Latchman and Aspinall, 2023).

Deformation monitoring conducted at La Soufrière showed two distinct phases of pre-eruptive deformation occurred (Camejo-Harry et al., 2023). The first is a deep source of inflation (~18 km depth) beginning 1st July 2020, and continuing into the effusive phase, ending in March 2021, recorded by the Global Positioning System (GPS) network. The second, occurring between 19th – 31st December 2020, a shallow source of inflation recorded by Interferometric Synthetic Aperture Radar (InSAR), was modelled to be an intrusive dike at depths of about 700-600 m (Joseph et al., 2022; Camejo-Harry et al., 2023).

Volatile concentrations (H_2O, CO_2, SO_2 and H_2S) in the plume were measured using Multi-component Gas Analyser System (MultiGAS) and Differential Optical Absorption Spectroscopy (DOAS) UV spectrometers were used to measured SO_2 fluxes (Joseph et al., 2022). The first gas measurements post-dome emplacement taken in January 2021 revealed no detectable SO_2 in the plume, and on 1st February, the first signal of SO_2 was detected by the MultiGAS (Joseph et al., 2022). Throughout the effusive phase, the MultiGAS ratios were indicative of deep magmatic and deep hydrothermal degassing (>10 km), except for one measurement taken on 23rd March, which indicates hydrothermal degassing, together with an increase in CO_2. Remote sensing 'traverses' were attempted using the UV spectrometer in January, February and March to obtain the SO_2 flux, however, no SO_2 was detected (Joseph et al., 2022). The change in the degassing signal from deep magmatic and deep hydrothermal magmatic to hydrothermal degassing was also coincident with a swarm of volcano-tectonic (VT) earthquakes occurred at depths <5 km on 23rd – 24th March, followed by a second swarm during 5th-6th April occurring at ~10 km depth. The swarm of deeper VTs was inferred to accompany a new batch of ascending magma (Joseph et al., 2022). Beginning on 8th April 2021, banded tremor for an interval of ~2.5 hours with increasing magnitude was recorded, consisting of multiple VT events. This progressed into continuous tremor with increasing amplitude (Joseph et al., 2022).

The first detection of SO_2 in the plume occurred on 8th April 2021 by DOAS and also by the TROPOspheric Monitoring Instrument (TROPOMI) on board the Sentinel-5 Earth observation satellite (Joseph et al., 2022; Esse et al., 2023) and roughly coincided with the emergence of banded tremor. The SO_2 flux measured on that day was 80 (±) 6 tonnes/day measured via ground-based traverses with a UV spectrometer (Joseph et al., 2022) or 121 (±) 86 tonnes/day as measured via TROPOMI (Esse et al., 2023).

Explosive Eruptions

On 9th April 2021, the eruption style of La Soufrière transitioned from lava effusion to a Vulcanian event, followed by a five-hour pause. After this, a series of near continuous sub-Plinian activity lasted until 10th April (Joseph et al., 2022; Sparks et al., 2023). Toward the end of 10th April, the style changed to discrete Vulcanian explosions, with increasing inter-explosive intervals, and a general decrease in both intensity and magma discharge rate, culminating on 22nd April, 2021 (Esse et al., 2023; Sparks et al., 2023). The transition in style from dome growth to explosions coincided with a rapid deflation of the volcano, modelled as the migration of ~50 x 10^6 m^3 of magma, from a storage region at ~6 km depth (Camejo-Harry et al., 2023). During the explosive phase, SO_2 emissions measured by TROPOMI were as high as 56 × 10^4 tonnes/day on 9th April (Esse et al., 2023), and as low as 331 tonnes/day as measured on 22nd April using DOAS (Joseph et al., 2022). Following the cessation of explosive activity on 22nd April 2021, seismicity decreased from an average of 354 events/day, to 24 events/day in early May 2021. Between May and November 2021, seismicity remained sparse (Joseph et al., 2022).

235

Methods and Materials

Sample Characteristics

The samples were collected from around La Soufrière during two field campaigns in January and May 2022 and were produced via Vulcanian and sub-Plinian eruptions from 9th–11th April 2021. During the explosive phase, seven stratigraphic units of material were produced and are described extensively in Cole et al., (2023). Of the seven units, units 1, 2, 3 and 5 contained vesicular scoria and are the focus of this study. The locations of sample collection and a brief description of each unit are outlined in Table 1 and Figure 1. Melt inclusions in the samples from the effusive phase (lava dome) were crystallised and were therefore not suitable for the methods employed in this study. Studying the uncrystallised melt inclusions in the scoria samples from units 1-3, and 5 allows for estimates of pre-eruptive volatile contents, and magma storage conditions (pressure and temperature).

La Soufrière melt inclusions are hosted in olivine, plagioclase, orthopyroxene and clinopyroxene phenocrysts. Plagioclase represents the greatest fraction of the phenocryst assemblage and crystals are typically euhedral, with lesser amounts of euhedral pyroxenes and subhedral olivine crystals. Phenocrysts appear as individual crystals, with small clusters and larger glomerocrysts present. Overall, the petrology of the samples studied is similar to scoria and dome samples from previous studies of the 2020-2021 eruption (e.g. Frey et al., 2023; Weber et al., 2023).

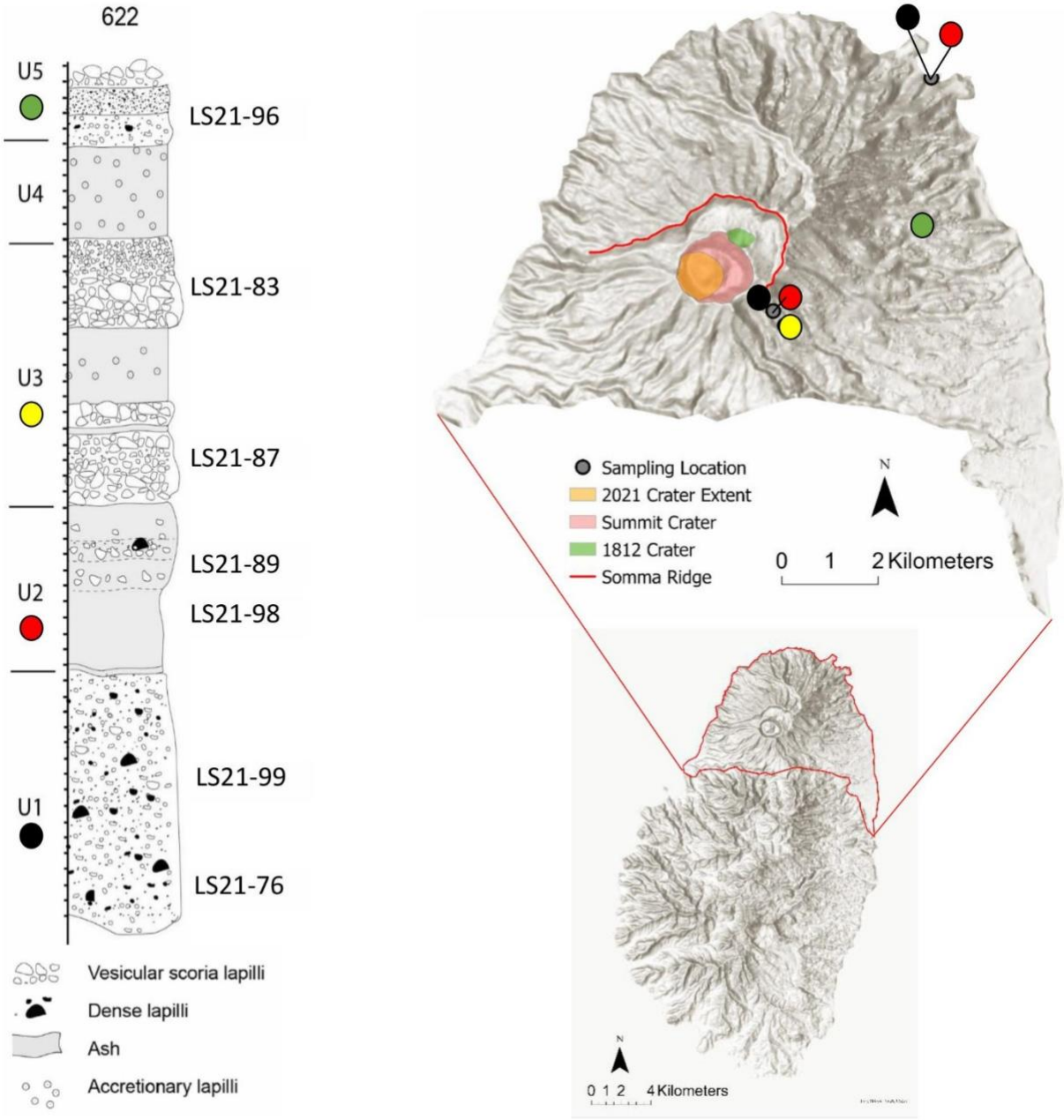

260

Figure 1: Stratigraphic column showing units 1 to 5 and samples used for analysis, and map of the La Soufrière edifice with sampling locations. Stratigraphic column from Cole et al., (2023). Topographic basemap from ESRI.

265 ## Sample Preparation

Scoria clasts from each unit were prepared for Raman spectroscopy, SIMS and EPMA by separating and crushing clasts using a mortar and pestle, and thensieving the material into different sized fractions. Olivine, plagioclase, orthopyroxene and clinopyroxene crystals were then hand-picked from the 250-500 µm and 500-1000 µm fractions under a binocular microscope. Crystals were individually mounted

on glass slides using Crystalbond 509 resin, lightly polished and inspected for non-crystallised melt inclusions (MI). Crystals containing appropriate melt inclusions were then polished using 2400 grade SiC paper and 3 and 1 μm aluminium oxide lapping paper, bringing the inclusion within~20 μm of the surface without exposing it, in order to avoid compromising the bubble for Raman analysis.

Melt inclusions (Figure 2) were glassy, with some, especially those hosted in pyroxenes, containing trapped pre-existing crystals such as iron oxides and/or daughter crystals grown from the melt after entrapment, and such inclusions were excluded from this study. Of 339 prepared melt inclusions, 336 contained bubbles. The 336 melt inclusions with bubbles occurred in three groups (Figure 2): (i) bubbles occupying <10% of the inclusion (76% of the population), (ii) bubbles occupying 10-60% of the inclusions (20% of the measured population), and (iii) multiple bubbles occupying a single inclusion (3% of the population). Inclusions hosted in olivine and pyroxene crystals displayed ellipsoidal shapes, whereas plagioclase hosted inclusions were predominantly cuboidal.

Following Raman spectroscopy, thirty-eight melt inclusions >25 μm (large enough to be analysed by SIMS) were polished further with 3 and 1 μm aluminium oxide paper, exposing the inclusion at the surface in order to measure the volatile elements CO_2, H_2O, S, Cl and F, and major elements in the glass by SIMS and EPMA. Samples were then removed from the glass slide and washed in an acetone bath to dissolve remaining resin.

Ahead of SIMS analysis, they were mounted in indium, oven-dried at 70°C, gold coated and equilibrated in the SIMS vacuum. Following SIMS analysis, the gold coating was removed with light polishing using a 0.25 μm diamond polishing pad and samples were carbon coated in preparation for EPMA.

Thirty-five additional inclusions between 10-25 μm were prepared for EPMA by polishing with 3 and 1 μm paper to expose the inclusion at the surface, removed from the glass slide and washed in an acetone bath. They were then embedded in a non-acetone soluble resin, placed in a 1-inch brass or aluminium holder and carbon coated in preparation for analysis.

Thin sections of scoria from each unit were prepares and carbon coated for EPMA in order to measure major and volatile (S, Cl, F) elements of the groundmass glass.

Five samples representative of the four scoria bearing units along with dense clasts of Unit 5 were crushed and sieved to 100 μm size, until 100 mg of powder was obtained, in preparation for ICP-OES.

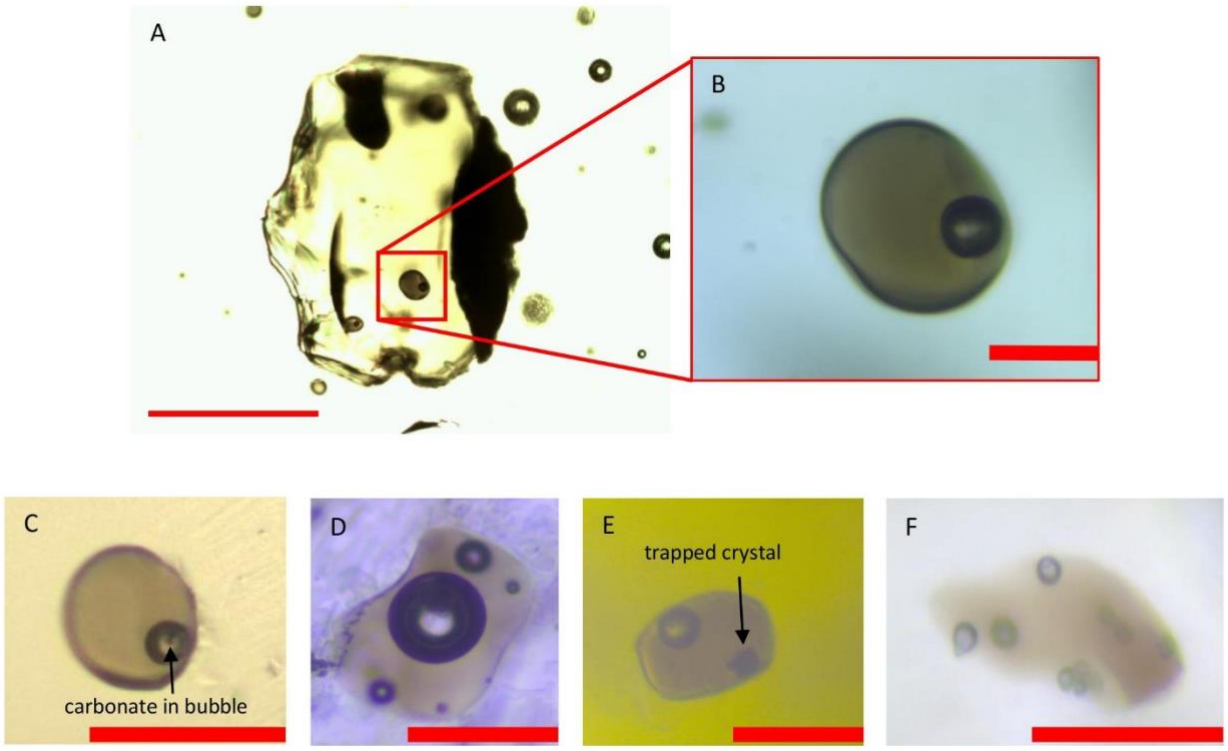

Figure 2 – Types of melt inclusions found in La Soufrière explosive products. [A] LSS_U3_OL_001 shows an olivine phenocryst hosting melt inclusions. [B] An ideal melt inclusion for this study with shrinkage bubble, crystal free glass, and sufficient diameter to accommodate SIMS and EPMA analysis. [C] LSS_U3_OL_001 - example of an inclusion with carbonate crystals in the bubble. [D] LSS_U2_PLAG_003_MI4 - example of an inclusion with large bubble >10% of inclusion volume along with multiple smaller bubbles. Due to high bubble volume ratio and irregularity in the glass, this is not ideal for analysis. [E] LSS_U1_CPX_010 is an example of an inclusion with a trapped crystal making it unsuitable for analysis. [F] LSS_U5_OL_025 is an example of an inclusion with multiple bubbles. Scale bar on [A] represents 200 µm. Scale bars on [B], [C], [D], [F] represent 50 µm. Scale bar on [E] represents 15 µm.

Analytical Techniques

Raman Spectroscopy

Raman spectra of individual bubbles were collected using a Renishaw inVia confocal Raman micro-spectrometer at Laboratoire Magmas et Volcans (LMV), Clermont-Ferrand, France in order to quantify the concentration of CO_2 sequestered, similar to Venugopal et al., (2020). The instrument was equipped with a 532.1±0.3 nm diode-pulsed solid-state laser delivering ~150 mW power to the sample, a Rayleigh rejection edge filter (cut-off at about 50 cm^{-1}), a CCD detector of 1040 × 256 pixels, a slit aperture of 20 µm (high confocality setting) and 2400 l/mm diffraction grating. The spectrometer uses a Leica DM 2500M optical microscope to focus on the sample; ×50 or ×100 microscope objectives were used, depending on the size of the bubble. These conditions result in a spectral resolution better than 0.4 cm^{-1}, and spatial resolutions of a few µm. This was paired with 10% laser power to avoid damaging bubbles close to the surface, allowing for repeated or additionalmeasurements. A higher laser power of 50% was used on occasion in an attempt to increase the Raman signal where necessary.

Each spectrum was collected in the 725-1880 cm^{-1} wavenumber range during 120 seconds of acquisition time (3 acquisitions of 40s), using the WiRE™ 4.4 software. This allowed for CO_2, which has two peaks at ~1285 and ~1388 cm^{-1}, dubbed the Fermi diad doublet, to be visible along with the peaks of the host phases. Identification of potential mineral phases, such as carbonates or sulphates, in bubbles required analysis in the 60-1320 cm^{-1} window. In a random selection of samples, an extended range was taken from 2400 to 4000 cm^{-1} in order to identify the presence of other liquid/gas species such as H_2S and HS^- (2550-2610 cm^{-1}) and H_2O at 2800-3900 cm^{-1}.

The 520.5 cm^{-1} peak of Si and two neon emission bands (568.982 and 576.442 nm) were used to perform the spectrometer alignment and to calibrate peak positions. Neon bands were measured prior to and after each acquisition, and the distance between the two emission lines (bracketing the Fermi diad) was used to calibrate the splitting of the Fermi diad. During the post-processing of the Raman spectra, a correction factor ($^{real}\Delta_{Ne}/^{measured}\Delta_{Ne}$) between 0.9990 and 1.0006 was applied to each measurement. To quantify CO_2 concentration in the bubbles, fluid inclusions standards of pure CO_2 of known densities were analysed three times during each analytical session. Uncertainties associated with the reproducibility of the measurement determined on standards are <0.04 g/cc. The errors associated with the measurement of CO_2 density in the studied bubbles are reported in Supplementary Material 2 and become relatively larger as CO_2 density decreases, mainly due to the greater uncertainty in the fitting of weak Raman peaks.

To calculate the concentration of CO_2 vapour sequestered within the bubble using mass balance equations (e.g. Hartley et al., 2014; Moore et al., 2019; Wieser et al., 2021), the volume fraction of the bubble within the melt inclusion and the density of the CO_2 vapour must be known. Volumes of both the bubble and the total inclusion were estimated using photomicrographs of the polished surface, assuming a spherical shape for the bubble, an ellipsoid for the melt inclusions hosted in olivine and pyroxene phenocrysts and a cuboid for plagioclase hosted inclusions, based on their 2D shapes. The x and y axes of melt inclusions were measured using a Leica DM4500 P LED microscope with Leica Application Suite software, with 0.2-micron uncertainty. The third unseen axis was calculated using the arithmetic mean of the x- and y-axis, which introduces a 5% error (with 1σ errors of -48 to 37%) on the calculation (Tucker et al., 2019). In order to calculate the density of CO_2 in bubbles (ρ_{CO_2}), each Raman spectrum was first processed using WiRE™ 4.4 spectral analysis program. Polynominal baselines were applied to spectra, which were truncated at 1200 and 1500 cm^{-1} to focus on the area known to contain the Fermi diad, and the peaks were fitted with a mixed Gaussian-Lorentzian curves. The centre of each peak was identified and the Fermi diad (Δ) calculated by subtracting their wavenumbers. The densimeter of Lamadrid et al., (2017) was used to calculate CO_2 density, as the instrument used does not have a specifically calibrated densimetry curve. The relationship between the Fermi diad (Δ) and CO_2 density (ρCO_2) is given by Equation 1:

.

$$\rho_{CO_2} = -39.737 + (0.387 * \Delta) \quad (1)$$

Fermi diad peaks with low intensity (<500 counts) or with asymmetrical peaks that evade ready curve-fitting could not be used to quantify ρ_{CO_2}, but were noted as they indicate a bubble containing a low density of CO_2 (Supplementary Material 2).

The CO_2 contribution from the bubble can therefore be calculated as the ratio of volume and density between the bubble and the glass using Equation 2:

$$[CO_2]_{bubble} = \frac{\rho_{CO2} V_{bubble}}{\rho_{glass} V_{glass}} \quad (2)$$

where $[CO_2]_{bubble}$ represents the increase in total inclusion CO_2 concentration resulting from CO_2 in the bubble. The volumes of the bubble and glass volumes are as previously defined.. The density of the glass is quantified with the DensityX model (Iacovino and Till, 2019) for one generic inclusion (LSS_U5_OL_003, Supplementary Material 2). Total CO_2 content of the melt inclusion is therefore the sum of the CO_2 in both the bubble and the glass.

H_2O and sulphur or carbon bearing species in the bubble identified by their Raman vibrations could not be quantified due to a lack of appropriate standards.

Secondary Ion Mass Spectrometry (SIMS)

SIMS analysis was carried out prior to EPMA in order to (i) avoid the contamination of C from the carbon coat necessary for EPMA, which makes the surface conductive and (ii) avoid beam damage in (especially hydrous) glasses due to EPMA which can cause the migration of mobile elements such as Na, K and H, and can also cause an increase in measured concentrations of immobile elements such as Si and Al (Humphreys et al., 2006; Rose-Koga et al., 2021).

The H_2O and CO_2 concentrations in thirty-eight melt inclusion glasses were measured at both the Natural Environment Research Council (NERC) Ion Microprobe Facility (IMF), University of Edinburgh, Scotland and at the Centre de Recherches Pétrographiques et Géochimiques (CRPG), Nancy, France.

The H_2O and CO_2 concentrations of melt inclusion glass from Unit 5 were measured at the NERC-IMF using a Cameca IMS 7f-GEO equipped with a 5 nA $^{16}O^-$ primary beam, resulting in a spot size of ca. 10×15 µm. Pressure in the chamber was 3.30 x 10^{-8} mbar. Samples were pre-sputtered for 180 seconds over an area of 25×30 µm for the removal of surface impurities before analysis. The isotopes of $^{24}Mg^{2+}$, $^{26}Mg^+$, and $^{30}Si^+$ were analysed with a counting time of 2 seconds per magnet cycle, whilst $^1H^+$ had a counting time of 3 seconds and $^{12}C^+$ of 10 seconds, averaged over 10 magnet cycles and counted using an electron multiplier. A mass resolving power of 1200 was used in order to separate the mass interferences of $^{24}Mg^{2+}$ and $^{12}C^+$. Background signals of $^{12}C^+$ and $^1H^+$ were measured using host phenocrysts and were subtracted from all analyses before final concentration calculations. MgO was measured to monitor possible overlap of the analytical spot with the host crystal. H_2O and CO_2 concentrations were calculated using the calibration curves (Figure S1, Supplementary Material 1) of $^1H^+/^{30}Si^+$ vs H_2O (wt.%) and ($^{12}C^+/^{30}Si^+$)*SiO_2 vs CO_2 (ppmw) for a set of known basaltic (N72, M5, M40, ALV519-4-1; Hauri et al., 2002; Shishkina et al., 2010) and rhyolitic (BF147, RB480, Sisson #48, Sisson #61, StHs6/80-G; Sisson and Grove, 1993; Brooker et al., 1999; Jochum et al., 2006) glasses analysed under the exact conditions of melt inclusion analysis, and SiO_2 is determined by EPMA subsequent to SIMS. The reproducibility of the standards (2σ) amounted to 10% for H_2O which has a detection limit of 0.01 wt.%, and 10% for CO_2 which has a detection limit of 60ppm.

At the CRPG facility, H_2O and CO_2 were measured in melt inclusion glasses from Units 1–3 using a Cameca IMS 1280 HR2 instrument which utilises a 10 kV Cs^+ primary beam with a current of 1 nA, coupled with an electron gun for charge compensation. H_2O and CO_2 were measured using a mass resolving power of ~7000 to separate mass interferences. Prior to analysis, an area of 15 x 15 µm was pre-sputtered for 300 seconds. Pressure in the chamber ranged from 1.1 x 10^8 to 1.0 x 10^8 mb over the analytical session. Background concentrations were measured using San Carlos olivine (Jarosewich et al., 1980) and were subtracted from all analyse prior to final concentration calculations. CO_2 concentrations were calculated using calibration curves (Figure S1, Supplementary Material 1) of CO_2 (ppm) vs ($^{12}C^+/^{30}Si^+$)*SiO_2 for several basalt (M35, M40, M43, M48, KL2-G, 40428, 60701, 47963, VG2; Jochum et al., 2006; Shishkina et al., 2010; Bindeman et al., 2012; Sobolev et al., 2016), andesite (T1-G; Jochum et al., 2006), dacite (StHs6/80-G; Jochum et al., 2006) and rhyolite (KE12) standards. Repeat analyses indicates a 2σ standard deviation dependent on CO_2 content. Reproducibility on standards with low CO_2 (~5 ppm) is <53%, while standards with higher CO_2 contents (hundreds to thousands of ppm) have a reproducibility of 20%, and the detection limit is 33 ppm. H_2O was calculated using the weighted mean of the two calibration curves of H_2O (wt.%) vs ($^{16}O^1H/^{30}Si$)*SiO_2 produced by basaltic (M35, M40, M43, M48, KL2-G, 60701, 47963, VG2, ALV1833-11, WOK28-3, CY82-31-2V; Hawkins et al., 1990; Stopler and Newman, 1994; Jochum et al., 2006; Shishkina et al., 2010; Bindeman et al., 2012; Sobolev et al., 2016) and rhyolitic (Panum-Dome, NW Coulee, MC84-df;

Newman et al., 1988; Hauri et al., 2002) glass standards, as a function of SiO_2. The reproducibility on the set of used standards is 5%, and the detection limit is 0.006 wt.%.

To compare H_2O and CO_2 measured in different labs, measurements were compared to M40 (Shishkina et al., 2010), an international standard of known composition used by both labs during the analytical sessions. The difference in H_2O for measurements of M40 at CRPG (3.28 wt.%) vs the known concentration (3.07 wt.%) amounts to 6%, while the difference for NERC (3.04 wt.%) vs M40 is 1%. The difference in H_2O for standard M40 measured at CRPG vs NERC is 7%. For CO_2, the difference between CRPG (2053 ppm) vs M40 (2183 ppm) is 6%, while NERC (2116 ppm) vs M40 (2183 ppm) is 3%, which demonstrates the coherence between our analyses in both laboratories. The difference between CO_2 values measured for M40 at CRPG vs NERC is 3%. Because all differences are <10%, H_2O and CO_2 from units 1-3 and unit 5 are directly comparable.

Electron Probe Microanalysis (EPMA)

The major element composition of crystals hosting melt inclusions, and major and volatile (S, Cl, F) element compositions of the inclusion glasses were measured using a Cameca SX-100 electron microprobe at the Laboratoire Magmas et Volcans, Clermont-Ferrand, France, with 15kV accelerating voltage (e.g. Kilgour et al., 2021). The conditions applied when measuring melt inclusion glasses consisted of a beam current of 4nA for major elements or 40 nA for volatile elements, paired with a defocused beam of 10 µm. In inclusions with limited glass surface area, a focused beam of 1 µm was applied. Two to three spot measurements per inclusion were taken in order to improve analytical precision in the relatively few inclusions that were sufficiently large. Detection limits for volatiles are 40 ppm for S, 49 ppm for Cl and 200 ppm for F. The compositions of olivine, plagioclase, orthopyroxene and clinopyroxene phenocrysts were measured using a 15nA beam current and focused beam pair. Additional information on standards used for calibration is given in Tables S1 and S2, Supplementary Material 1. The 2σ uncertainty for major elements based on known standards is <5% for SiO_2, Al_2O_3, FeO and CaO, <10% for TiO_2 and MgO, 11% for Na_2O and 20% for K_2O. The 2σ uncertainty for volatile element compositions based on repeat measurements on the inclusion was 35% for S, 6% for Cl and 44-61% for F depending on F content.

Inductively Coupled Plasma Optical Emission Spectrometry (ICP-OES)

The major elements of whole rock samples from U1, U2, U3 and U5 were determined using an Agilent 5800 ICP-OES instrument at the Laboratoire Magmas et Volcans, Clermont-Ferrand France.

One hundred mg of each sample were melted together with three times the amount of $LiBO_2$ in an induction furnace at 1100°C for five minutes, after which, the melted product was dissolved in 1 M HNO_3, until a final volume of 200 ml was achieved. Standards used for reference are the granite 'GH' for Si, Na and K, and the basalt 'BR' for Al, Ti, Fe, Mn, Mg, Ca and P, provided by CRPG, Nancy, France. The associated uncertainty was less than 10% (2σ).

Results

Whole rock composition

Scoria produced in the 2021 explosive eruption are basaltic andesite in composition with 53.6 – 54.8 wt.% SiO_2 (Table S3, Supplementary Material 1), comparable to analyses of Joseph et al., 2022. They overlap with historical and pre-historical eruptions, although whole rock analyses from the suite of historical and pre-historical eruptions spanned a wider compositional field (Figure 3; from Graham and Thirlwall, (1981); Heath et al., (1998); Cole et al., (2019); Fedele et al., (2021).

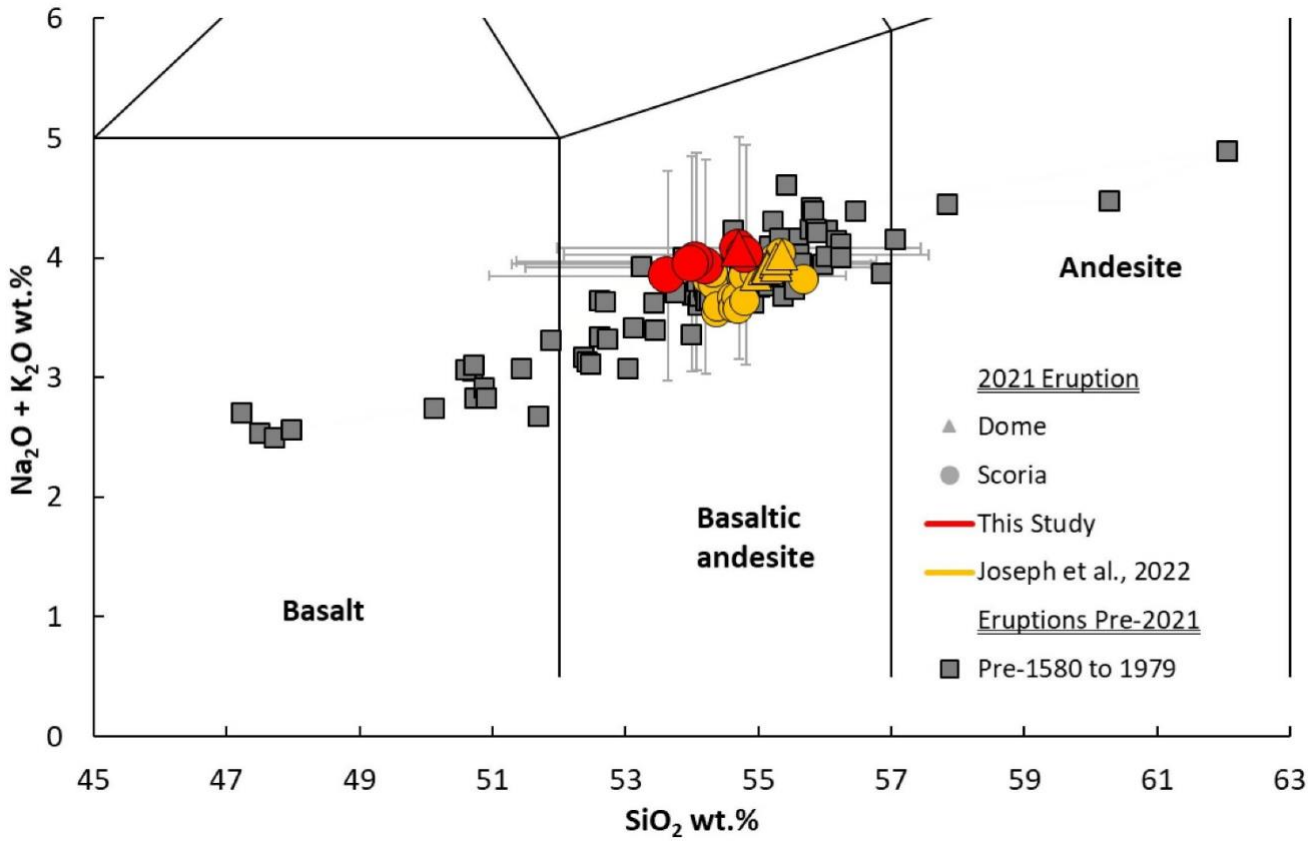

Figure 3: Total Alkali vs Silica (TAS; Le Bas et al., 1986) plot showing the basaltic andesite composition of the 2020-2021 whole rock products in comparison to historic and pre-historic compositions compiled from Graham and Thirwall, (1981); Heath et al., (1998); Cole et al., (2019); Fedele et al., (2021).

Host compositions and texture

Compositions of olivine hosts of select melt inclusions considered in this study range from Fo_{65-76}, indicating evolved crystals, similar to the 1979 (Fo_{64-77}) and pre-historic eruptions (Fo_{55-85}) of La Soufrière (Graham and Thirwall, 1981; Heath et al., 1998). There is no significant difference between forsterite (Fo) contents of olivine phenocrysts in different units, however, two groups exist within the olivine population – the first being Fo_{72-76}, accounting for 81% of analysed phenocrysts, and the second group being Fo_{65-69}, accounting for 19% of the population (Figure 4). Twenty-four of twenty-eight crystals are in equilibrium with the whole rock total K_D range = 0.25–0.43 (K_D is described in the following section), whereas none are in equilibrium with the groundmass glass (total K_D range = 0.07–0.16) which has an average composition (Frey et al., 2023) equivalent to rhyolite. In comparison, olivine phenocrysts display <5 μm wide rims of different Fe contents than the cores (Frey et al., 2023)

Plagioclase compositions are similar across units 1–3, with anorthite (An) contents ranging from An_{65-95}. There are no plagioclase compositions available for unit 5. They comprise normally zoned crystals with high anorthite cores ($An_{>80}$), becoming less calcic towards the rim, down to An_{60}. Oscillatory zoning on the spatial scale of tens of microns is also present and occurs in mostly normally zoned crystals that can be either high- or low-An ($An_{65–75}$). Eight of ten melt inclusions measured for volatiles were located in high An zones, with no difference observed in volatile content based on melt inclusions local An content. Eleven of nineteen plagioclase hosts are in equilibrium with the whole rock, with a total K_D range of 0.03–0.44, and five of nineteen are in equilibrium with the groundmass glass based on K_D for temperatures <1050 °C.

Two pyroxene groups exist in the La Soufrière explosive products, each having narrow compositional ranges in enstatite (En) content. Orthopyroxenes range from En_{63-67} while clinopyroxenes range from En_{41-43}. 25% of orthopyroxenes are in equilibrium with the whole rock, having a total K_D range of 0.30 – 0.43. Clinopyroxenes, however, are all in equilibrium with the whole rock, having K_D between 0.24 and 0.34. This is in agreement with textural indicators of equilibrium, such as sharp euhedral edgesin unzoned ortho- and clinopyroxenes (Frey et al., 2023). Neither pyroxene group is in equilibrium with the groundmass at K_D 0.11-0.17 for orthopyroxene and 0.07-0.13 for clinopyroxene. Orthopyroxenes have Mg# [$(Mg/Mg+Fe^{2+})*100$ moles] of 65 – 72, whilst clinopyroxenes Mg# are 71 – 76.

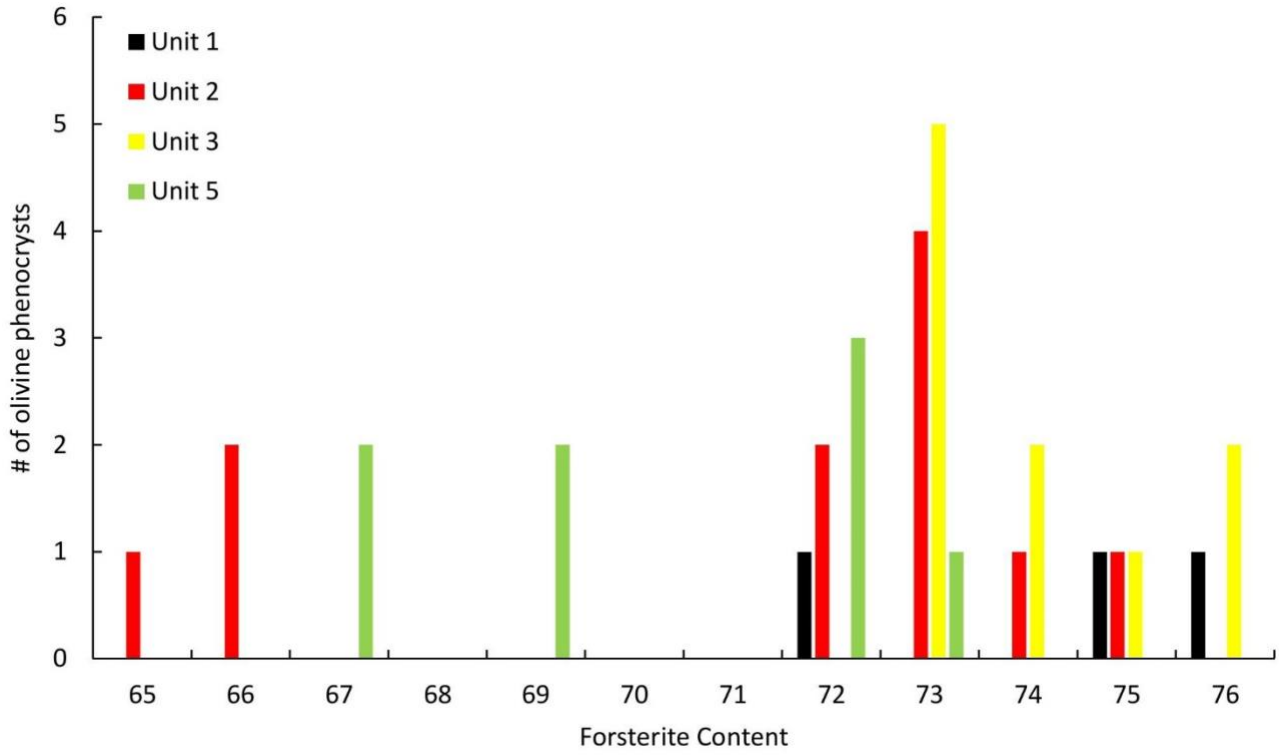

Figure 4 – Population of La Soufrière olivines showing two groups: Fo_{72-76}, accounting for 26 of 32 analysed phenocrysts, and Fo_{65-69}, accounting for 7 of 32 analysed phenocrysts.

Melt inclusion compositions

Post-entrapment modification and reconstruction

Melt inclusions that have undergone post-entrapment modification follow a separate evolution trend to their parent magma outside of the host crystal. This includes diffusion of water into or out of inclusions (Gaetani et al., 2012), post-entrapment crystallisation and melting (PEC; Kent, 2008), diffusion of major elements compatible to the host (Kent, 2008), volatile loss due to decrepitation (Neave et al., 2017), growth of crystals from the inclusion melt before quenching, or the formation of vapour bubbles (Steele-Macinnis et al., 2011; Moore and Bodnar, 2019). These processes can change the original composition of the melt, in both major/minor elements and volatile species. Therefore, assessment of the degree of modification is required prior to using the data in geochemical and petrological models.

Post-Entrapment Crystallisation

The extent of post-entrapment modification of olivine-hosted melt inclusions was assessed by calculating equilibrium between each olivine-melt pair using the $K_D{}_{ol-liq}^{Fe-Mg}$ model of Toplis (2005). At La Soufrière, olivine-liquid pairs are in equilibrium at K_D = 0.33±0.02. Further testing for Fe/Mg

diffusion showed Fe loss in some inclusions when compared to the La Soufrière whole rock and groundmass glass liquid line of descent (LLD; Graham & Thirlwall, 1981; Heath et al., 1998, Cole et al., 2019; Fedele et al. 2019). When inclusion-host pairs are in equilibrium, the inclusion undergoes minimal PEC, and the measured glass composition closely reflects the melt composition at the time of entrapment (Putirka, 2008). $K_{D_{ol-liq}}$ for this suite of La Soufrière melt inclusions ranges from 0.13-0.30, indicating PEC, with some inclusions experiencing Fe loss, as FeO contents are ~2wt.% lower than the LLD (Figure S3, Supplementary Material 1).

All olivine-hosted melt inclusions were corrected for both post-entrapment crystallisation/melting and Fe-Mg exchange using MiMiC (Rasmussen et al., 2020).This was done by incrementally adding or subtracting olivine from the inclusion until equilibrium was achieved between the melt and the host olivine, based on the initial FeO content estimated from the LLD. PEC required the addition of 0.60–6.79 wt.% olivine to achieve equilibrium, while post-entrapment melting required the subtraction of 0.28–3.92 wt.% olivine. Corrected compositions are presented in Supplementary Material 2.

Assessment of equilibrium between orthopyroxene-liquid pairs, which is obtained at $K_D{}^{Fe-Mg}_{px-liq} = 0.29 \pm 0.06$ (Putirka, 2008), was carried out using Fe-Mg ratios between the host crystal and the melt inclusion. While Fe-Mg exchange can occur in pyroxene-melt pairs, diffusion through pyroxene crystals is slower than that of olivine (Müller et al., 2013; Dohmen et al., 2016). Orthopyroxene-hosted inclusions had K_D of 0.13–0.25, and those out of equilibrium (six of nine inclusions) were corrected for PEC by incrementally adding orthopyroxene back into the inclusion until $K_D{}^{Fe-Mg}_{px-liq}$ of 0.29 was achieved. All reconstructed inclusions now fit the trend of the LLD. Reconstructed inclusions required the addition of 3.10–6.45% orthopyroxene to achieve equilibrium.

Experimental data show that clinopyroxene-liquid pairs are in equilibrium at $K_D{}^{Fe-Mg}_{px-liq} = 0.28 \pm 0.08$ (Putirka, 2008). Measured K_D was 0.12–0.24, with eight of seventeen clinopyroxene-inclusion pairs being within equilibrium range. Inclusions out of equilibrium with their hosts were therefore corrected for PEC by incrementally adding the clinopyroxene until $K_D{}^{Fe-Mg}_{px-liq} = 0.28$, and predicted and observed clinopyroxene components (DiHd, EnFs, CaTs, Jd, CaTi, CrCaTs) were within 15%. This required the addition of 7.3-13% of clinopyroxene. Corrected compositions are presented in Supplementary Material 2.

In plagioclase-liquid pairs, an indication of post-entrapment crystallisation is the resulting increase in MgO and decrease in Al_2O_3 in inclusions (e.g. Nielsen, 2011) in relation to an established LLD. At La Soufrière, plagioclase hosted inclusions can be divided into two groups, based on PEC and diffusion of elements. The first defines a group at $K_2O<1.0$, consisting of 14 inclusions. Harker plots of Al_2O_3 vs

K_2O and MgO vs K_2O indicate that this group is characterised by low Al_2O_3 (up to 3 wt.% lower than the trend exhibited by olivine- and pyroxene-hosted inclusions; Figure S4, Supplementary Material 1) and high MgO (up to 3 wt.% higher), indicating PEC. However, two inclusions fall within the accepted K_D range given by Putirka (2008). The second group consists of six inclusions at >1.0 K_2O. In this group, four of five inclusions are in the accepted K_D range, and all fall within the trend exhibited by olivine- and pyroxene-hosted inclusions. Inclusions were assessed for PEC based on the Al_2O_3-K_2O relationship defined by olivine and pyroxene hosted melt inclusions (Figure S4), regardless of equilibrium state. Plagioclase (9.88–23.53) was incrementally added back into inclusions until Al_2O_3 values equalled the predicted value at a given K_2O based on regression data (R^2=0.62). The plagioclase-liquid model of Namur et al. (2012) was used.

Bubble growth

The growth of bubbles in melt inclusions occurs as a result of changes in the pressure, volume and temperature in the liquid-host crystal system, with contributing processes including PEC, H^+ loss from the inclusion, and differing thermal expansivities of the host and inclusion (Roedder, 1979; Anderson and Brown, 1993; Lowenstern, 1995; Kent, 2008; Wallace et al., 2015; Hanyu et al., 2020). Bubble growth can sequester large amounts of volatiles trapped in inclusions. Up to 99% of CO_2, 60% of S and 16% of H_2O has been found to be held in melt inclusion bubbles as vapour or as an aqueous solution, as well as major and minor elements which together with volatile elements forms solids in the form of carbonates, sulphates and other mineral groups (e.g. Moore et al., 2015; Esposito et al., 2016; Schiavi et al., 2020; Venugopal et al., 2020; Howe et al., 2025). Therefore, element diffusion into the bubble has the ability to affect a range of magma and magma storage properties.

The population of 394 measured bubbles in the La Soufrière melt inclusions can be divided into two groups: (i) those with a discernible Fermi diad (vapour bubble CO_2), accounting for 7% of the population, and (ii) those without a Fermi diad (the remaining 93%). Raman spectra with low counts (<500) and those with skewed peaks unsuitable for mixed Gaussian-Lorentzian curve fitting could not be used to accurately calculate CO_2 densities or concentrations and so are not considered. All melt inclusions with a discernible Fermi diad contain a singular bubble.

A total of 394 analysed bubbles across the four units were found to have a wide range of sizes, accounting for <1–32% of total inclusion volume (Figure S7, Supplementary Material 1). To ascertain which bubbles were formed post-entrapment, the model of Moore et al., (2015) was used. The volume change in inclusion glass and host crystal were calculated using average inclusion compositions in each host type, along with entrapment temperatures (see section 5.1.1) and glass transition temperatures of 425–450°C, calculated using melt viscosity models (Giordano et al., 2008). For olivine-hosted inclusions at La Soufrière, olivine contracts by 2% and the melt by 8% at a calculated glass transition temperature of 440°C. This allows for the growth of a bubble occupying 6% of the inclusion volume.

Similar calculations for plagioclase- orthopyroxene and clinopyroxene-hosted inclusions indicate that homogenously grown bubbles should occupy 6%, 4% and 5% of the melt inclusion volume respectively. Therefore, melt inclusions with bubbles larger than this 4-6% volume threshold (10 of 29 bubbles) are likely trapped melt and vapour already present in bubble(s) entrapment, and adding their CO_2 to the measured glass values would lead to an overestimation of the CO_2 content of the melt at the time of entrapment. Orthopyroxene-hosted inclusions are calculated to grow the smallest bubbles, as the inclusions are generally more evolved, and therefore contract less during cooling than the lesser-evolved olivine-hosted compositions. Across the four units, bubble volume is predominantly 1-3%, particularly in unit 5 (Figure S7, Supplementary Material 1). This shows that the majority of bubbles were grown from the same process of differential thermal contraction, with others showing evidence of bubble growth and entrapment. Bubble sizes range from <1–32% in Unit 1 (100 bubbles; mean = 5±5%), 1–24% (86 bubbles; mean = 4±4%) in Unit 2, 1–25% in Unit 3 (69 bubbles; mean = 6±6%), and <1–14% (88 bubbles; mean = 4±3%) in Unit 5.

Since no bubbles in melt inclusions analysed by SIMS contained CO_2, the total CO_2 used in models from this point forward is equivalent to the CO_2 measured in the glass. However, we recognise that a small proportion of the melt inclusion bubbles that were analysed by Raman spectroscopy but not SIMS did contain measurable CO_2, and we therefore consider the glass-only CO_2 concentrations measured by SIMS to be minimum values.

The 29 bubbles yielding measurable Fermi diads have CO_2 densities ranging from 0.003–0.147 g cm^{-3} (Figure S5, Supplementary Material 1). As the measured densities are less than the critical density of CO_2 (0.468 g cm^{-3}; Moldover, 1974), the bubbles contain CO_2 purely in the vapour phase, and CO_2 is therefore not underestimated due to the presence of a liquid phase. CO_2 densities across all units are similar.

Unit 1 has the widest range of CO_2 densities, from 0.003–0.147 g cm^{-3}, with twelve bubbles presenting Fermi diads, while in Unit 2, five bubbles have measurable CO_2 densities of 0.023–0.086 g cm^{-3}. There was only one bubble in Unit 3 presenting a Fermi diad, with measured CO_2 density of 0.028 g cm^{-3}. Unit 5 had six bubbles with densities spanning 0.004–0.126 g cm^{-3}. No correlation is observed between CO_2 density and bubble volume (Figure S5, Supplementary Material 1).

Additionally, there is no distinction between bubbles containing vapour CO_2 and carbonates and bubbles with only vapour CO_2, suggesting insignificant CO_2 precipitation as carbonates (Figure S5, Supplementary Material 1). Carbonates were identified in twenty-eight of three hundred ninety-four bubbles analysed and were present in all crystal phases and units. In unit 1, seven bubbles contained carbonates. In unit 2, there were ten, and in units 3 and 5, there were four and seven bubbles containing carbonates respectively. However, carbonates could occur on the rim of other bubbles, as a comprehensive characterisation of solid phases was not conducted and is outside the scope of this

research. Carbonates occur in the form of calcite, nahcolite, natrite, and gaylussite, identified by their main and other vibrations (Frezzotti., et al., 2012) during Raman spectroscopy. It is important to note that carbonates were present in both bubbles with and without Fermi diads, indicating that the amount of CO_2 measured in the bubble should be considered minimum values.

Along with CO_2 and carbonates, other volatile species in the form of gases, solids and solutes were present in bubbles at La Soufrière. H_2O was present in twelve bubbles from all four units, in both aqueous and gaseous phases. This includes three inclusions measured for H_2O at the SIMS - two hosted in olivine – LSS_U1_OL_003 (aqueous H_2O) and LSS_U2_OL_006 (aqueous H_2O), and one hosted in clinopyroxene – LSS_U3_CPX_007 (gaseous H_2O). While the sequestration of H_2O into these three bubbles may lead to an underestimation of H_2O concentrations in the surrounding glass, the measured H_2O contents still fall e within the range defined by other, non-bubble bearing H_2O samples. Sulphur bearing species in the form of H_2S vapour and HS^- and H_2S dissolved as solutes in water were also present in seven bubbles from unit 1, 3 and 5, including two samples measured with EPMA. These two samples yielded glass S concentrations that were within range of those for non-bubble bearing inclusions. Raman peaks at 984 and 1000 cm^{-1} likely indicate the presence of sulphates in two olivine hosted inclusions in unit 3 (Frezzotti et al., 2012).

Major element composition

Seventy-eight La Soufrière melt inclusions show compositional variation from basaltic (48.5 wt.% SiO_2) to andesitic (61.6 wt.% SiO_2), except for two dacitic inclusions. Overall, there are two groups of data separated by a compositional break between 0.6-0.8 wt.% K_2O (Figure 5). Olivine hosted inclusions exist at lower K_2O (<0.6 wt.%), are the least evolved being basaltic to andesitic in composition (48.5–57.5 wt.% SiO_2). Conversely, those inclusions in the group >0.8 wt.% K_2O contain the most evolved inclusions and are orthopyroxene-hosted, ranging from andesitic to dacitic in composition (58.1–65.1 wt.% SiO_2). In these inclusions, the lowest Mg# corresponds with the highest SiO_2. Plagioclase and clinopyroxene-hosted inclusions span both low and high K_2O groups, where the plagioclase-hosted inclusions are basaltic to dacitic, with 50.1–63.4 wt.% SiO_2, whilst clinopyroxene-hosted inclusions span a narrower compositional range from basaltic andesite to andesite at 54.3-61.4 wt.% SiO_2).

Major element oxides are plotted against K_2O because of its incompatible behavior in most magmatic systems, which makes potassium a useful proxy for magma differentiation. No clear compositional trends exists between units (Figure 5). In all melt inclusions, SiO_2, Na_2O and P_2O_5 increase with K_2O, whereas Al_2O_3, FeO, MgO, CaO decrease. TiO_2 and MnO remain relatively constant with increasing K_2O. The major element compositions of melt inclusions hosted in olivine, plagioclase and clinopyroxene overlap with those of whole-rock sample. In contrast, groundmass glass

compositions (Frey et al., 2023) represent the final stages of crystallisation, and reach a maximum SiO_2 content of 69.31 wt.%. Melt inclusions that are in equilibrium with their host, and those corrected for PEC are detailed in Supplementary Material 1.

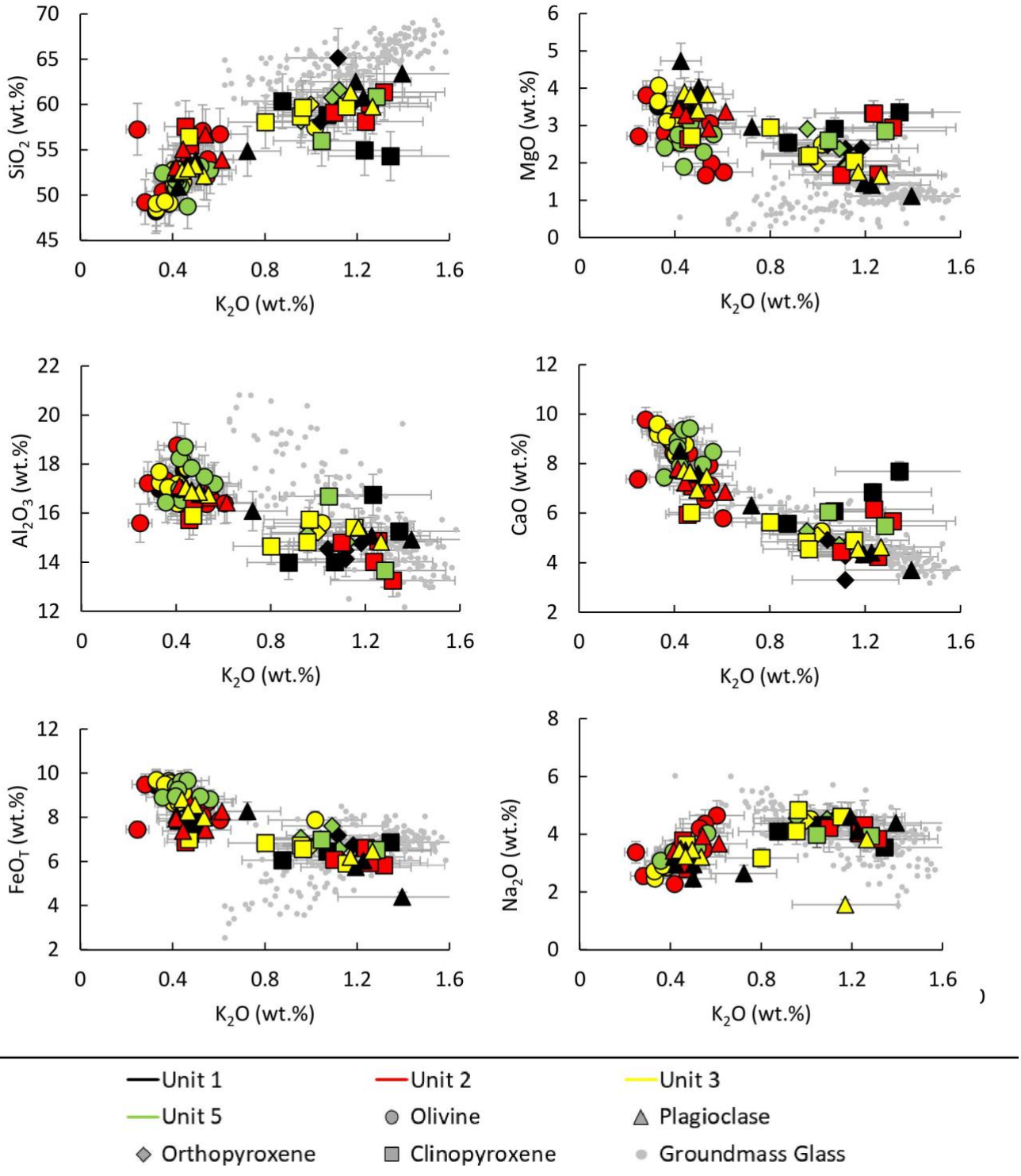

Figure 5: Major element compositions versus K_2O for La Soufrière melt inclusions showing a compositional gap between ~0.6–0.8 wt % K_2O. Groundmass glass are plotted as grey circles, showing compositional evolution and is from Frey et al., (2023) for the 2021 eruption. Where error bars are not shown, the associated error is smaller than the symbol.

695

Volatile element composition

The volatile contents in La Soufrière melt inclusions are comparable to other Lesser Antilles Arc volcanoes (e.g. Mann et al., 2013; Gurenko et al., 2005) and volcanoes from other arcs (Wallace, 2005). On average, La Soufrière melt inclusions contain 4.25 ± 0.76 wt.% total volatiles. Three of the four most primitive inclusions (3.65 – 4.08 wt.% MgO) have a complete volatile dataset (CO_2, H_2O, S, Cl, F) comprising 5.40 ± 0.05 wt.% total volatiles.

Melt Inclusion Glass

705

H_2O and CO_2

H_2O contents in thirty-nine melt inclusions across the four units vary from 2.61–5.37 wt.% (Figure 6), making up the majority of dissolved volatiles. These concentrations are comparable to published values of 4.90 – 5.30 wt.% for St Vincent products (n=3; Cooper et al., 2020) and 0.83-5.23 wt.% for primitive melt inclusions (Bouvier et al., 2008; Bouvier et al., 2010). However, they exceed the 1.5-3.9 wt.% estimated using the volatile by difference method for plagioclase and pyroxene hosted melt inclusions (Weber et al., 2023; e.g. Humphreys et al., 2006) and the 2.8-3.1 wt.% estimated based on plagioclase microlite hygrometry (Frey et al., 2023). H_2O decreases with increasing K_2O (Figure 6) and the highest H_2O concentrations occur in olivine-hosted inclusions (3.42–5.37 wt.%, n=18), which also have the least evolved compositions, whereas plagioclase-hosted inclusions contain 2.61-4.11 wt.% (n=10). The two pyroxene phenocrysts have similar H_2O contents – orthopyroxene with 3.34–3.66 wt.% (n=2) and clinopyroxene with 3.10–4.51 wt.% (n=9). There is no distinct trend between erupted units, however the presence of two compositional groups are also evident where H_2O contents show a decrease with increasing K_2O up to 0.6 wt.%, while they remain constant for K_2O >0.8 wt.% (Figure 6). H_2O contents are taken as representative of the magma at melt inclusion entrapment, and there is no evidence of H_2O loss by diffusion across the observed range of K_2O concentrations.

CO_2 concentrations in 29 melt inclusions hosted in all four crystal phases generally range from 3–661 ppm (Figure 6). Two inclusions, however, have much higher CO_2, of >2000 ppm. One olivine-hosted inclusion has 2506 ppm CO_2, and one plagioclase-hosted inclusion 3567 ppm. There are no trends in CO_2/K_2O, and no significant differences between units, as Unit 1 CO_2 ranges from 8–661 ppm, Unit 2

3–434 ppm, Unit 3 12–139 ppm (3567 ppm if the two >1000 ppm outliers are taken into consideration), and Unit 5 20–162 ppm (Figure 6). Twenty-eight of twenty-nine melt inclusion glass concentrations represent the total CO_2 in the inclusions at trapping, as their bubbles lacked Fermi diads or carbonates. Sample LSS_U3_OL_011_MI2 lacked CO_2 in its bubble, but the presence of carbonate was detected. Unlike H_2O, there does not appear to be a clear difference in CO_2 contents at high and low K_2O groups, however, the low K_2O group contains the two highest measurements.

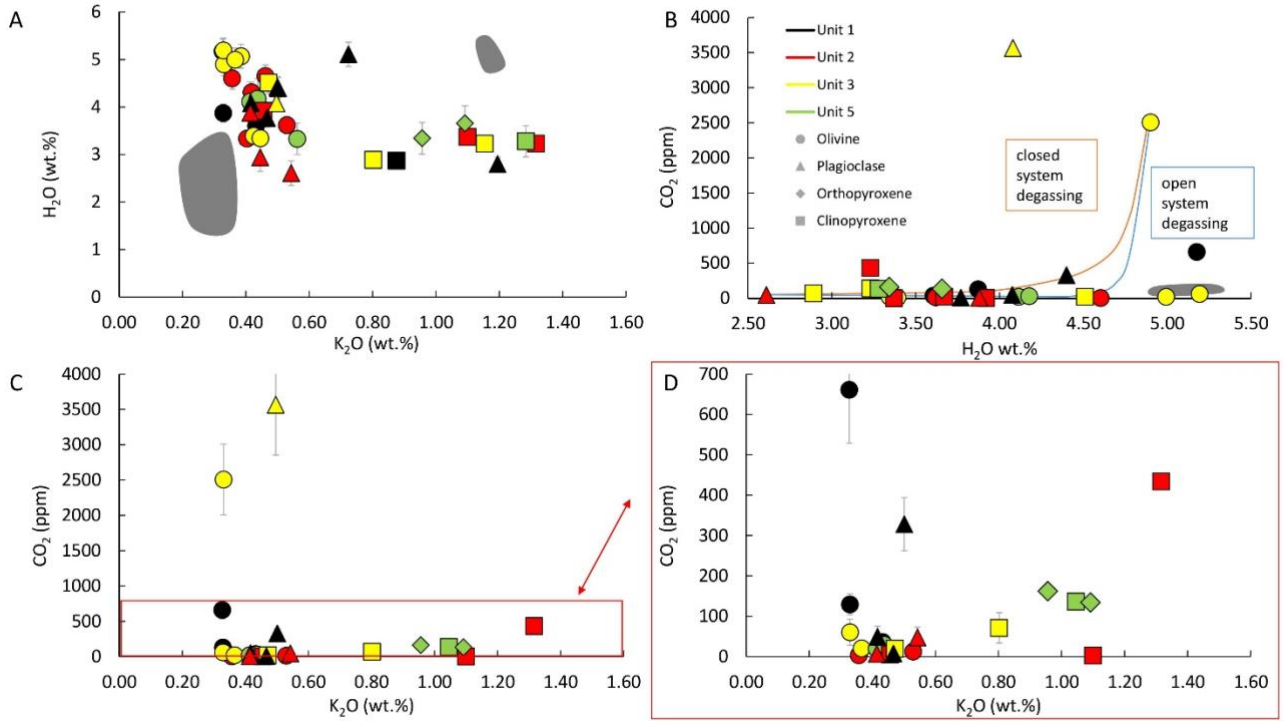

Figure 6: H_2O and CO_2 in La Soufrière melt inclusions. [A] H_2O vs K_2O showing degassing up to ~0.6 K_2O after which the trend levels. [B] CO_2 vs H_2O does not follow simple open- and closed-system degassing trends modelled using melt inclusion LSS_U3_OL_003 which had high CO_2 and H_2O. [C] CO_2 vs K_2O indicates very low CO_2 in the majority of inclusions and no systematic variation in CO_2 with K_2O. Degassing paths modelled using VESIcal (Iacovino et al., 2021) [D] CO_2 vs K_2O at CO_2 values up to 700 ppm as an extension of panel [C]. Error bars are 2σ, and where error bars on [A], [B] and [C] are not shown, the associated error is smaller than the symbol. Grey shaded areas represent published values from Bouvier et al., (2008); Bouvier et al., (2010) and Cooper et al., (2020).

Sulphur (S), Chlorine (Cl) and Fluorine (F)

Sulphur contents in seventy-four inclusions range from 59–836 ppm. In all units, S decreases with increasing K_2O (Figure 7a) and concentrations are generally consistent between units. However, a compositional discontinuity is observed; inclusions with lower K_2O exhibit higher S contents and a steep S/K_2O gradient, whereas those with higher K_2O show lower S contents and a shallower gradient. The highest S concentrations are also measured in olivine-hosted inclusions, ranging from 162-620 ppm, with one outlier inclusion at 836 ppm. Lower S concentrations occur in melt inclusions within other crystal hosts, with ranges from 92–285 ppm for plagioclase, 90–306 ppm for orthopyroxene, and

59–293 ppm for clinopyroxene-hosted inclusions. Sulphur concentrations in melt inclusions from the 2021 explosive eruption of La Soufriere are broadly consistent with the only previously published data for this system – from the 1979 eruption – where S ranged from below the detection limit (<50 ppm) to 558 ppm at K_2O concentrations of 0.45-0.96 wt.%. Within the Lesser Antilles arc, S concentrations in La Soufrière melt inclusions are comparable to those reported for volcanoes such as South Soufrière Hills Volcano, Montserrat (Cassidy et al., 2015) and La Soufrière de Guadeloupe, Guadeloupe (Metcalfe et al., 2023), where S also ranges from below detection limit to ~780 ppm. These volcanic systems are all more S-rich than both Soufrière Hills Volcano, Montserrat (Edmonds et al., 2001) and Morne Trois Pitons-Micotrin, Dominica (d'Augustin et al., 2020) where maximum S is ~70 and ~150 ppm respectively.

Cl behaves incompatibly, with concentrations rising as magma differentiates, as indicated by the overall positive trend of Cl vs K_2O (Figure 7b). Cl vs K_2O in olivine (Figure 7b circles) has a strongly positive correlation (R^2 of 0.91). However, there is a decrease in the gradient of Cl vs K_2O in plagioclase, orthopyroxene and clinopyroxene hosts, particularly above 0.8 wt.% K_2O, as well as a wider variation in the data (Figure 7b). The trend also highlights two groups of melt inclusions as seen in other elements. In Cl, concentrations increase in the low K_2O group, and after the compositional gap at 0.6-0.8 wt.% K_2O, Cl values become more stable. This trend is also seen in pre-historic La Soufrière inclusions (Heath et al., 1998). Overall, Cl concentrations span 981–5083 ppm, comparable to values from pre-historic eruptions of La Soufrière (Heath et al., 1998; Bouvier et al., 2010), and other Lesser Antilles volcanoes more broadly (e.g. Edmonds et al., 2001; Gurenko et al., 2005; Metcalfe et al., 2023).

Similarly, fluorine generally increases with K_2O up to 0.6 wt %, after which the concentration remains stable in the >0.8 wt.% K_2O group (Figure 7c). F concentrations in all melt inclusions range from below detection limit to 880 ppm, roughly comparable to pre-historic La Soufrière eruptions (100-1600 ppm; Heath et al., 1998; Figure 7c) and to other Lesser Antilles volcanoes where F concentrations reach up to 500 ppm (Edmonds et al., 2001; d'Augustin et al., 2020; Metcalfe et al., 2023).

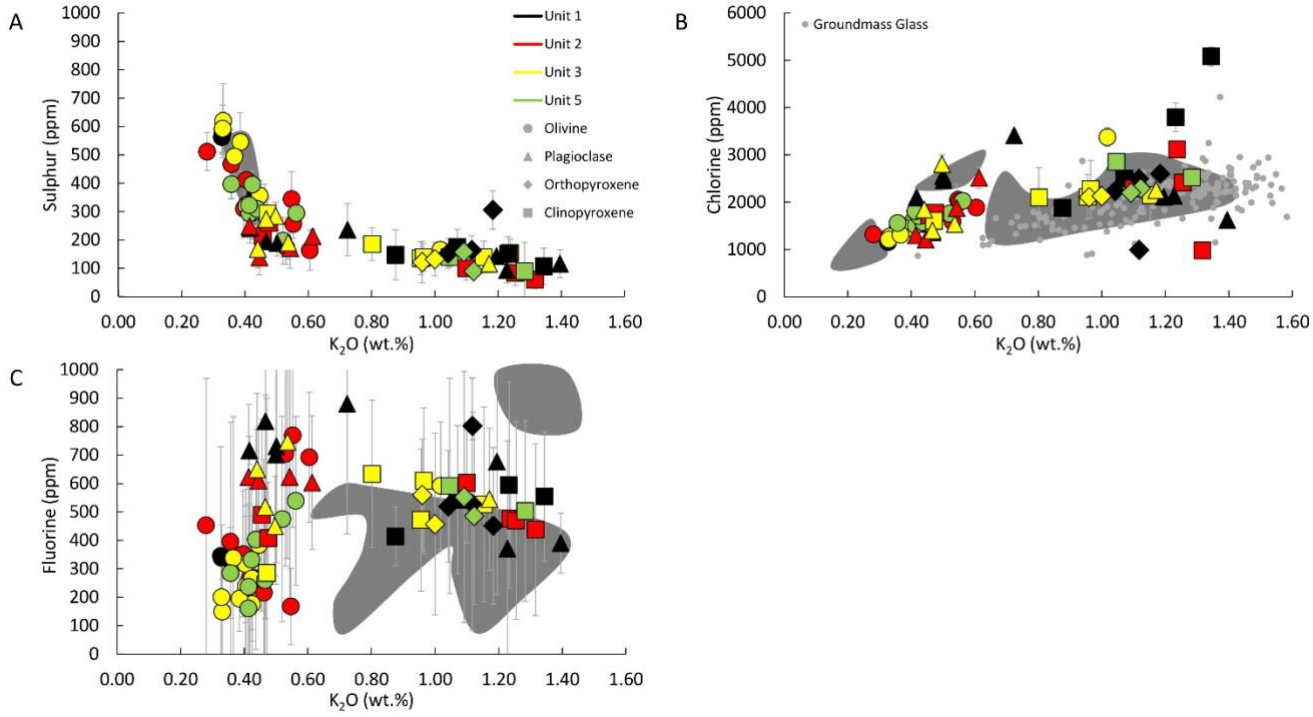

Figure 7: Sulphur and halogen compositions of La Soufrière melt inclusions. [A] Sulphur vs K_2O exhibiting degassing behaviour. Areas shaded in grey are compositions measured in products from the 1979 eruption from Devine and Sigurdsson, (1983). [B] Chlorine vs K_2O shows a steady increase between K_2O of 0.2-0.6, after which the gradient of increase decreases and becomes less correlated. Grey circles are groundmass glass compositions for the 2021 explosive products from Frey et al., (2023). Grey shaded areas are pre-historic melt inclusions from Heath et al., (1998) and Bouvier et al., (2010). [C] Fluorine vs K_2O also showing an increase from 0.20-0.60 K_2O, followed by a decrease in F content. Grey shaded areas are pre-historic melt inclusions from Heath et al., (1998) and Bouvier et al., (2010) which generally overlap with 2021 inclusions. Error bars are 2σ and where error bars are not shown, the error is smaller than the symbol.

Melt Inclusion Bubble

Mass balance calculations show that bubbles in La Soufrière melt inclusions contain 68 – 1807 ppm CO_2 (Figure S6, Supplementary Material 1). In Unit 1, the eight inclusions that pass the bubble volume threshold test have CO_2 concentrations of 72 – 1014 ppm. Unit 2 bubbles are within similar range, with four bubbles ranging from 205 – 1007 ppm. The lone Unit 3 bubble has a concentration of 572 ppm, whilst five such bubbles in Unit 5 range from 68 – 1807 ppm. Of these eighteen bubbles which grew homogenously in the inclusion, twelve contain CO_2 higher than that measured in the glass. However, these bubbles were hosted in inclusions that were not acceptable for SIMS analysis due to small size or

the presence of crystals. We are therefore unable to calculate total CO_2 for these 28 melt inclusions and their CO_2 concentrations are minimum values due to unmeasured CO_2 in the glass.

Discussion

Magma Storage Conditions

CO_2 solubility in magma is pressure-, temperature- and major element composition-dependent. Several models exist, allowing for calculation of magma storage conditions from melt inclusions such as melt inclusion entrapment pressure, based on CO_2-H_2O systematics (e.g. Newman and Lowenstern, 2002; Ghiorso & Gualda, 2015; Allison et al., 2022). To do this, the total CO_2 concentration (bubble + glass) in melt inclusions must be known. Several studies have highlighted the fact that shrinkage bubbles can contain up to 99% bulk melt inclusion CO_2 content (e.g. Hartley et al., 2014; Moore et al., 2015; Aster et al., 2016; Venugopal et al., 2020; Howe et al., 2025) leading to an underestimation if only glass-held CO_2 is considered.

Several inclusions contain multiple bubbles, often with small diameters <10 μm (e.g. LSS_U5_OL_025_MI2 containing nine bubbles, all <7 μm). This suggests that the melt was

supersaturated in volatiles, leading to a high nucleation rate. However, in the 2021 explosive eruption at La Soufrière, no CO_2 was detected in 93% of bubbles. This could be due to a number of possibilities; either (i) bubbles contained low-density CO_2 vapour undetectable by the instrument, however, this is highly dependent not only on the analytical conditions used, but also on the phase hosting the sample, depth of bubble beneath the surface as well as size of the bubble, (ii) bubbles grew by differential thermal contraction followed by rapid cooling, which provided insufficient time for CO_2 diffusion into the bubble, resulting in the formation of vacuum bubbles (e.g. Schipper et al., 2010; Steele-Macinnis et al., 2011), (iii) CO_2 vapour present in bubbles crystallised to form carbonates (e.g. Schiavi et al., 2020), although carbonates only appear in a small percentage (7%) of La Soufrière inclusions, or (iv) CO_2 was lost due to decrepitation (e.g. Maclennan, 2017). Given the low detection limit for CO_2 vapour by Raman spectroscopy and the fact that there are carbonates in some bubbles, rapid cooling prohibiting diffusion of CO_2 into bubbles (theory ii), vapour CO_2 crystallising to form carbonates (theory iii), or decrepitation upon migration into a lower pressure storage region (theory iv) are all possible explanations for the presence of empty bubbles.

After correction for post-entrapment processes (uncorrected and corrected compositions listed in Supplementary Material 2), melt inclusion H_2O, CO_2 and major element compositions can be used to estimate magma storage conditions such as temperature, pressure and inferred depth, and thus better constrain magma generation, evolution and differentiation processes.

Temperature

Magmatic temperatures were calculated for olivine-, plagioclase-, orthopyroxene- and clinopyroxene-hosted melt inclusions across the four scoria-bearing units using several different geothermometers. These are shown in Figure 8. Temperatures of olivine-hosted melt inclusions were calculated using the MgO thermometer of Sugawara, (2000), built on experimental results showing a linear relationship between mol% MgO and temperature. This method is associated with a standard estimate of error (SEE) of 30 °C. Temperatures of plagioclase-hosted inclusions were assessed using two methods. Firstly, the thermometer of Waters and Lange (2015) was used to assess magmatic temperatures of the ten plagioclase-hosted inclusions for which H_2O was measured by SIMS, as plagioclase composition is strongly dependent on magma H_2O content (Waters and Lange, 2015). Secondly, plagioclase-liquid thermometry was used, based on Equation 24a from Putirka, 2008 (SEE 36°C). Temperatures for nine orthopyroxene hosted inclusions were calculated using Equation 28a of Putirka, 2008 (SEE 28 °C), based on orthopyroxene-liquid equilibria. Clinopyroxene-liquid thermometry based on Putirka, (2008) Equation 33 (SEE 45 °C), was applied to seventeen inclusions. Overall, temperatures for the 2021 explosive eruption (970-1120 °C) generally overlap with calculated temperatures of the 1979 and pre-historic eruptions (1000-1180°C; Devine and Sigurdsson, 1983; Bardintzeff, 1984; Martin-Lauzer et

al., 1986; Heath et al., 1998). However, it is noted that similarly to the major and volatile elements, there are two groups of temperatures – higher temperatures associated with the olivine and plagioclase hosted melt inclusions, and lower temperatures associated with the pyroxene-hosted melt inclusions.

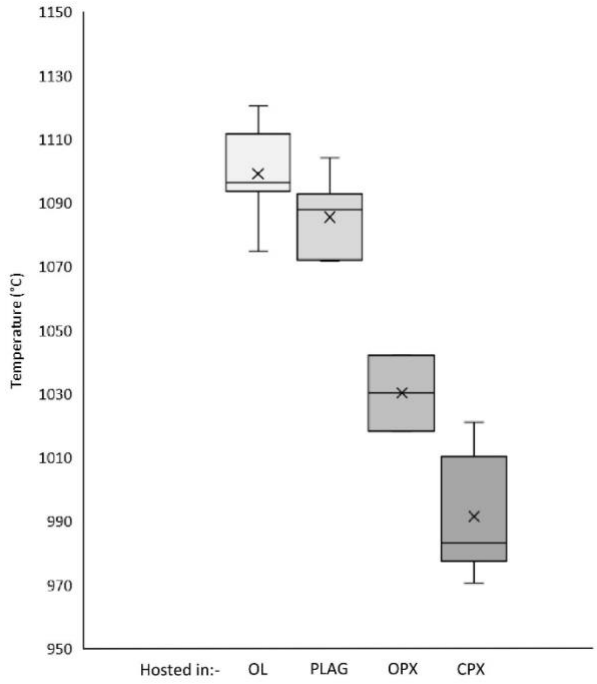

Figure 8: Box and whicker plot of calculated temperatures for the explosive products of the 2021 eruption based on host crystal phase. Olivine-hosted (OL) melt inclusions yield the highest temperatures, followed by plagioclase-hosted (PLAG), orthpyroxene-hosted (OPX) and clinopyroxene-hosted melt inclusions (CPX). The whiskers extend from the box and represent the extent of the dataset while the box represents the upper and lower quartiles. The horizontal line inside each box represents the median, and the 'x' represents the mean of the dataset.

Saturation Pressures and Depths

Melt inclusion entrapment pressures were estimated using the H_2O-CO_2 solubility model MagmaSat (Ghiorso and Gualda, 2015), hosted in VESIcal (Iacovino et al., 2021), assuming (i) vapour saturation, as H_2O and CO_2 do not behave compatibly based on their relationship with K_2O and (ii) that post-entrapment modifications such as bubble formation, PEC, and H_2O loss are accounted for, as discussed previously. Based on melt inclusion composition, H_2O and CO_2 contents, and temperature, entrapment pressures yield 100±10 to 230±22 MPa for olivine-hosted, 62±9 to 160±19 MPa for plagioclase-hosted, 110±16 to 120±18 MPa for orthopyroxene-hosted, and 85±12 to 160±20 MPa for clinopyroxene-hosted inclusions, where uncertainties are 2σ on each minimum and maximum value (Figure 9). Two outliers are present for olivine- and plagioclase-hosted inclusions at 320±33 to 620±88 MPa.

Inferred entrapment depths beneath the surface for the La Soufrière melt inclusions were calculated assuming a crustal density of 2660 kg m^{-3}, based on gravity modelling data for the Lesser Antilles crust (Christeson et al., 2008). Twenty-five of twenty-eight inclusions yield depths of 2.4±0.3 to 8.9±0.9 km depth (mean 6.4 km), with one inclusion at 12±1.3 km depth, and two high CO_2 inclusions at 21±2.5 and 24±3.4 km depth (Figure 9). While the mean depth of the entire melt inclusion population is 6.4±4.8 km, there are two discrete groups of melt inclusions that can be distinguished using major elements (Figure 5), volatile elements (Figure 6; Figure 7) and temperature data (Figure 8) presented here, and also seen in the petrology of the 2020/2021 eruptive products (Frey et al., 2023; Weber et al., 2023). It is proposed, based on an extensive range of methods (e.g. experimental petrology, mineral petrology, xenolith petrology, geophysical studies) applied to various eruptions and their products from pre-historic to present times, that the La Soufrière plumbing system consists of two main magma storage regions situated at ~6 km and 13-20 km depths (Tolan et al., 2011; Fedele et al., 2021; Camejo-Harry et al., 2023; Latchman and Aspinall, 2023), where the deep region is dominated by a basalt-basaltic andesite melt, and the shallow region by andesite-dacite melt within a crystal mush (Weber et al., 2023). The volatile-derived melt inclusion entrapment depths here mostly coincide with residence in the shallower storage region, with some inclusions sampling the deeper region.

As discussed above, our melt inclusions have likely been altered by processes such as decrepitation, leading to CO_2 loss from the melt inclusion. Here, we model two scenarios: First, in order to model pressures at entrapment, and prior to decrepitation, we use average and maximum measured CO_2 concentrations in the 18/394 bubbles grown post-entrapment (based on bubble volume fraction), where a Fermi diad was present, indicating CO_2 (Supplementary Material 2). Here, we find that when an average CO_2 concentration (472-875 ppm across the units) from bubbles is added to that of the glass, saturation pressures increase from 110 to 370 MPa (from 4 to 14 km depth). Using the maximum CO_2 concentration in these bubbles, (1014-1807 ppm), saturation pressures further increase up to 430 MPa or 17km depth. This addition of CO_2 to the glass of our melt inclusions correspond with the deeper storage region at 13-20 km (Fedele et al., 2021; Camejo-Harry et al., 2023; Weber et al., 2023), showing that some melt inclusions were indeed trapped in the deeper storage region before migration to the shallow region where decrepitation took place due to the pressure change. This, together with the presence of carbonates in empty bubbles further solidifies the hypothesis of CO_2 loss from bubbles. Secondly, we model minimum saturation pressures using the 18 bubbles grown post-entrapment for which CO_2 was present (Supplementary Material 2), but which were unsuitable for SIMS in order to calculate the total CO_2 content of the melt inclusion, thus providing minimum pressures only. Since we lack analytical data for the glass component for these bubbles, we use average temperatures, H_2O contents and major element compositions per host phase in our calculations of saturation pressure. We

estimate minimum pressures of entrapment for these 18 bubbles at 100-360 MPa, corresponding to depths of 3.9-14.6 km (Figure 9).

To further investigate the inferred depth of melt inclusion entrapment and depths of crystallisation using their measured compositions, we compare volatile solubility relationships with independent depth constraints from clinopyroxene-only barometry and liquid-crystal equilibria. Clinopyroxene-only barometry is carried out using two barometers. Firstly, Equation 30 of Putirka, (2008) enables direct comparison with values published by Weber et al., (2023). This model yields pressures of 350-530 MPa (6.1-20.3 km) for sixteen clinopyroxene compositions, in comparison to 280-400 MPa (10.7-15.3 km) reported by Weber et al., (2023) assuming a crustal density of 2660 kg m^{-3} (Christeson et al., 2006). The two datasets largely overlap, and there is no significant difference as the root mean square error (RSME) on this method is 450 MPa or 17.2 km depth (Wieser et al., 2021). We also use the clinopyroxene-only barometric model of Wang et al., (2021) Equation 1, which is appropriate for clinopyroxenes crystallized in melt containing <60 wt.% SiO_2. This applies to 15 of the 17 crystals analysed, and yields a lower uncertainty of ±180 MPa (6.9 km). The two remaining crystals are associated with more evolved melt inclusions, with SiO_2 contents of 60-61wt.%.. Clinopyroxene-only barometery on all 17 crystals, using Equation 1 of Wang et al., (2021), yield pressures of 30-210 MPa (average 110 MPa), corresponding to depths of 1.1-8.0 km (average 4.2 km), with the two inclusions >60 wt.% SiO_2 also falling within this range. These depths are much lower than the results using Equation 30 of Putirka, (2008), but are within error, and match more closely with the volatile-derived pressure/depth constraints. We therefore rely on the Wang (2021) model, and deduce that the majority of clinopyroxene crystallisation occurred in the shallow storage region between 4-6 km depth.

We additionally employ liquid-crystal equilibria to identify the melt composition in equilibrium with the remaining host minerals and thus provide additional constraints on the magmatic plumbing system. Weber et al., (2023) infers an andesitic-dacitic carrier melt, with 60-64 wt.% SiO_2 based on mass balance calculations on phase proportions, whole rock, groundmass glass, melt inclusions and mineral chemistry. Here we apply orthopyroxene-liquid equilibria to whole rock compositions (basaltic andesite) and groundmass glass (andesite to dacite). Equilibrium is achieved between an andesitic (62 wt.% SiO_2) liquid and six of nine orthopyroxene crystals. The remaining three crystals are in equilibrium with a basaltic andesite liquid (54 wt.% SiO_2). These results, together with the low calculated temperatures for orthopyroxene-hosted melt inclusions (1018-1042 °C), indicate that orthopyroxene most likely crystallised in the cooler andesitic reservoir situated at shallow depths similarly to the clinopyroxene (based on clinopyroxene compositions).

Plagioclase-liquid equilibrium models are applied to nineteen low ($An_{<80}$) and high ($An_{>80}$) anorthite plagioclase-whole rock and plagioclase-groundmass glass pairs to test chemical equilibrium.

Eleven of fourteen high An plagioclase crystals are in equilibrium with a basaltic andesite melt, whereas the five low An plagioclases are all in equilibrium with an andesite liquid. This suggests that high An plagioclases predominantly derive from the deeper, hotter basaltic andesite reservoir, while low An plagioclases formed in the shallow, cooler andesitic reservoir.

Chemical equilibrium is tested between twenty-eight olivine-liquid pairs in the average whole rock and andesite compositions as above. The overwhelming majority (26) are not in equilibrium with an andesitic melt, while 17 of 28 are in equilibrium with a basaltic-andesite melt. Based on the high temperatures yielded, textural disequilibrium in the whole rock shown by thin rims of differing compositions than cores (Frey et al., 2023) and the chemical equilibrium test, we ascribe olivine crystallisation to the deeper, hotter basaltic-andesite storage region.

In summary, our melt inclusion and mineral dataset indicate two separately crystallising magma bodies forming a transcrustal mush system beneath La Soufrière volcano (Figure 9). Between July and December 2020, there was the injection of magma into a storage region 18±1.9 km inferred from GPS and InSAR deformation data (Camejo-Harry et al., 2023). Over the next 3-9 months, high An plagioclase and olivine crystallised from this deep, hotter melt in the mid-lower crust region, while the shallow, cooler, andesite crystal mush in the upper crust crystallised low An plagioclase along with clinopyroxene and orthopyroxene. In the weeks leading up to the transition from effusive to explosive activity, there is seismic evidence of migration of magma into the base of the shallow reservoir at ~7-8 km depth (Latchman and Aspinall, 2023). This was then followed by syn-eruptive deformation modelled by GPS and InSAR during the explosive phase at ~6 km depth (Camejo-Harry et al., 2023). We acknowledge that despite the overwhelming evidence for polybaric crystallisation, there is a surprising lack of melt inclusions clustered at ~18 km on Figure 9. Instead, the entire melt inclusion dataset clusters around 6 km, with only three inclusions spread between 12-24 km. We attribute this to decrepitation led volatile loss from the melt inclusion after upward migration and stalling of the deeper magma, which erased the deep CO_2 signature in particular.

While clinopyroxene barometry using Equation 1 from Wang et al., (2021) fits the volatile data presented here, it is associated with large errors that span much of the upper crust (Wieser et al., 2023). Therefore, we emphasise the importance of using H_2O-CO_2 solubility constraints to estimate the depth of magma storage. Although we recognize that this relationship may be affected by re-equilibration processes, H_2O-CO_2 contents reflect the final depth of magma storage prior to eruption. This study provides the first pressure and depth estimates based on H_2O-CO_2 solubility at La Soufrière volcano, offering a valuable independent constraint on magma storage conditions within the crust.

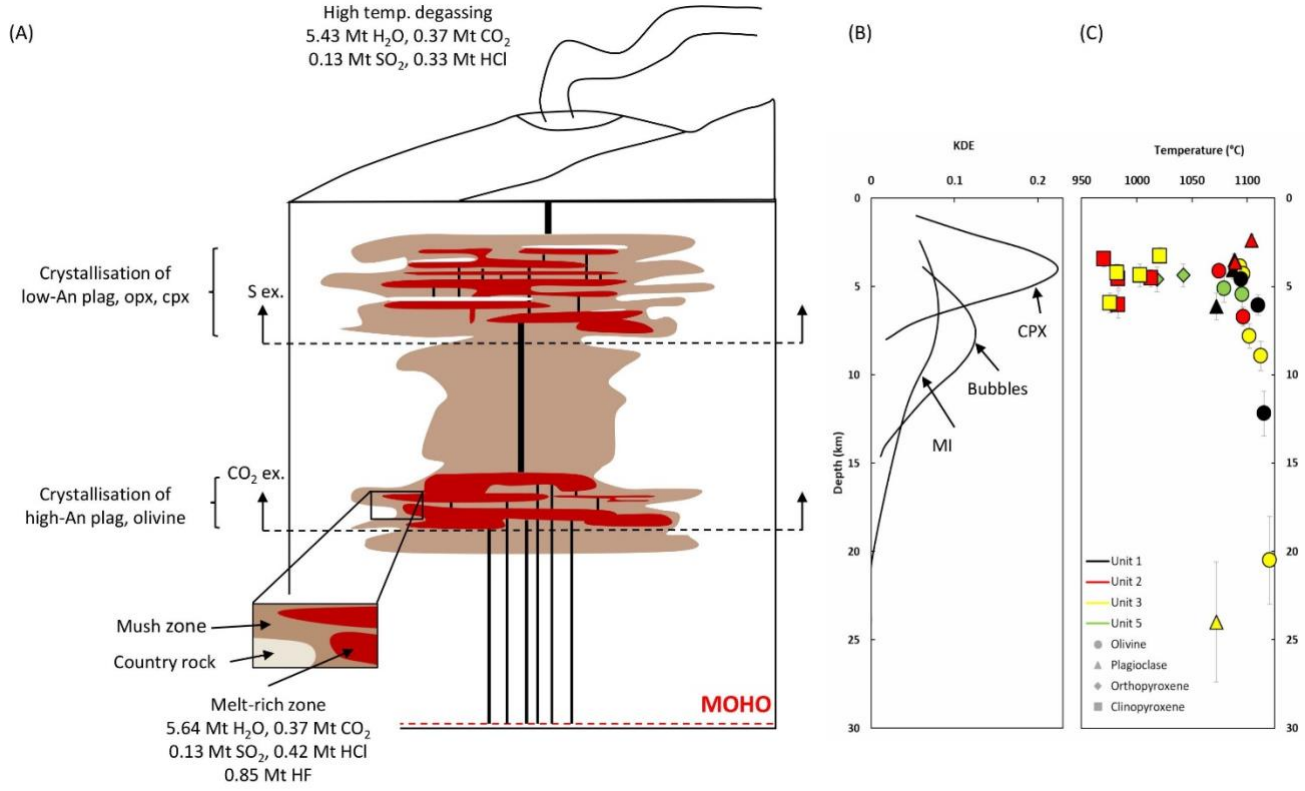

Figure 9: (A) Schematic of the La Soufrière volcano plumbing system showing a polybaric transcrustal mush system where high-anorthite plagioclase and olivine crystallises at depths situated around 18 km, and low-anorthite, orthopyroxene and clinopyroxene crystallises at shallow levels <8 km. CO_2 exsolution depths (18 km) and S exsolution depths (8.4 km) are also shown. (B) Kernel density estimates (KDE) show depths yielded from clinopyroxene-only barometry, depths calculated using the 18 bubbles grown post-entrapment which contained CO_2 but were not measured at SIMS/EPMA, and also shows the depths of melt inclusions for which H_2O and CO_2 were measured in the glass, but has empty bubbles due to decrepitation upon ascent to the shallow reservoir. (C) The temperature vs depth plot shows saturation pressures based on H_2O-CO_2 solubility.

Magma Degassing

The solubility of S in the melt, like that of H_2O and CO_2, depends on parameters such as pressure, temperature, H_2O content and major element composition, but also on sulphur and oxygen fugacity, which dictates its dissolving speciation (Carrol and Webster, 1994; Liu et al., 2007; Jugo, 2009; Li et al., 2021). The compositional effect is particularly important, where S exists primarily as sulphide (S^{2-}) in reducing conditions, and as sulphate (S^{6+}) in oxidizing conditions (Wallace and Carmichael, 1994; Jugo et al., 2005). The presence of S^{2-} vs S^{6+} determines the magmatic sulphur content at sulphide saturation (SCSS) which buffers the carrying capacity of the magma with respect to sulphur, and can result in S contents that diverge from fractional crystallisation trajectories (and reduces the availability of initial S to be degassed). Experiments show that the transition from S^{2-} to S^{6+} is determined by oxygen fugacity, and occurs between FMQ and FMQ+2 (FMQ refers to the fayalite-magnetite-quartz buffer;

Jugo et al., 2009; Symthe et al., 2017; O'Neill, 2021). This means that in S^{6+} dominated systems, the SCSS is higher than in S^{2-} dominated systems (Jugo et al., 2005).

For this suite of La Soufrière melt inclusions, sulphide saturation occurs between 172 and 806 ppm using the model of Li et al., (2021) which is appropriate for La Soufrière as it takes into consideration hydrous magmas, covers a wide range of compositions, accounts for both sulphide and hydrosulphide species and is based on a thermodynamic approach rather than empirical regressions. Taking the model results into consideration, only six of twenty-nine melt inclusions (Figure 10A) for which we have measured H_2O achieved sulphide saturation (since SCSS is affected by melt H_2O content; Li et al., 2021) and melt inclusion compositions in Figure 10A are clearly not buffered along the SCSS. However, S and H_2O are positively correlated (Figure 10B), demonstrating degassing of both volatiles with no differences between units 1-5, and the data also shows no departure from the trend (e.g. decreasing S at fixed H_2O), suggesting that S was not lost to a sulphide phase. The maximum measured H_2O content of 5.19 wt.% and S concentration of 620 ppm are therefore considered minimum values for the parental magma.

We also investigate S degassing using Sulfur_X (Ding et al., 2023) which predicts the equilibrium melt and vapour compositions for multi-volatile systems (CO_2, H_2O, SO_2 and H_2S) under closed-system degassing using Iacono-Marziano et al., (2012) H_2O-CO_2 solubility model and the S-speciation model of O'Neill and Mavrogenes, (2022). We model S degassing for our suite of melt inclusions and find that S began to degas at a pressure of ~220 MPa or 8.4 km depth at La Soufrière (approximate base of the upper crystallising body based on H_2O-CO_2 solubility calculated in the Saturation Pressures and Depths section) and that by 5 km depth, the magma lost ~60% of its S.

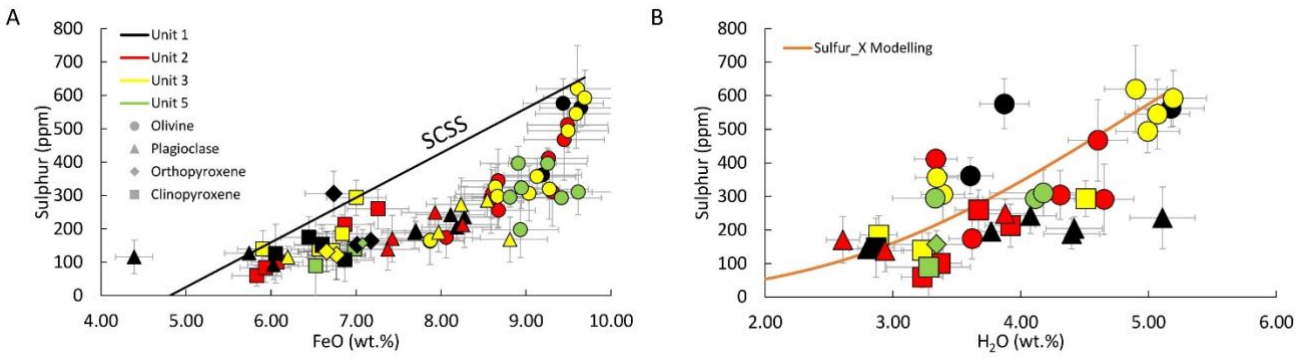

Figure 10: [A] Sulphur vs FeO for this suite of melt inclusions from the 2021 explosive phase of La Soufrière volcano exhibiting an increasing trend of S with FeO under oxidising conditions. [B] Sulphur vs H_2O showing an overall degassing trend of both volatile species, and modelling of sulphur degassing using Sulfur_X (Ding et al., 2023).

Sulfur_X is also used to compare CO_2/S_T ratios measured in the plume with CO_2/S_T ratios from this suite of melt inclusions to model the pressure-dependent evolution of the magmatic gas phase upon their migration and decompression (e.g. Burton et al., 2007; Aiuppa et al., 2017). The molar ratios of CO_2/S_T at La Soufrière (where S_T is the total sulphur, achieved by summing $SO_{2(g)}$ and $H_2S_{(g)}$) were measured using a MultiGAS in 2018 (Joseph et al., 2022), and ranged from 22-36. Following the extrusion of the lava dome in the 2020/2021 eruption, the MultiGAS was deployed for the first time at La Soufrière since 2018, and during the effusive phase, measurements covered a wide range of ratios from 9-75 (14th January to 23rd March 2021; Joseph et al., 2022). Models were run without any crystallisation, thus allowing a single melt composition during decompression, except for Cluster 3B (Table 2).

We present five models in order to represent the range of pressures and depths obtained from melt inclusion H_2O-CO_2 solubility relationships (Figure 11; Table 2). Cluster 1 represents the group of melt inclusions with low CO_2 plotting at an average of ~5 km depth. The second cluster represents inclusions in the intermediate-depth group, plotting at ~9 km, and the third cluster represents the group of inclusions plotting in the lower crust at ~22 km (Figure 9). Average compositions of H_2O, CO_2, S and temperature are calculated for Clusters 1, 2, 3A and 3B and all parameters are listed in Table 2. Cluster 3C represents the olivine hosted melt inclusion (LSS_U3_OL_003) in the 22 km group which has the highest S in the dataset (Table 2). All models were ran at ΔFMQ of +2.08 as defined for the La Soufrière system by Bouvier et al., (2008).

High CO_2/S_T plume ratios can occur as a result of a lack of detectable SO_2 in the plume following the scrubbing effect into the hydrothermal system (Joseph et al., 2022), they therefore do not represent gas chemistry at depth. In order to compare CO_2/S_T ratios modelled using our melt inclusion dataset to CO_2/S_T emitted via the plume, we use the lowest ratio to combat contamination of the scrubbing effect.

As shown in Figure 11, Clusters 1 and 2 show melt saturation pressures at ~160 and 230 MPa respectively, however, CO_2/S_T ratios modelled in melt inclusions from these groups do not correspond to ratios in the plume. This indicates that these Clusters consist of melt inclusions that have already lost considerable CO_2 and S.

In Cluster 3, all three models show melt saturation at >350 MPa. Taking into consideration the scrubbing effect, the lowest ratio of 9 measured on February 1st 2021 suggests equilibrium pressures between 140 and 190 MPa or 5.4 and 7.3 km depth. This depth range broadly agrees with our estimates of the shallow reservoir depths at 1.1-8.0 km obtained using clinopyroxene-only barometry, and 2.4-

8.9 km obtained using melt inclusion H_2O-CO_2 barometry. The CO_2/S_T modelling results further validates the use of these melt inclusion compositions as the degassed magma and further strengthen the evidence that all melt inclusion-hosted minerals resided in the upper crust prior to eruption.

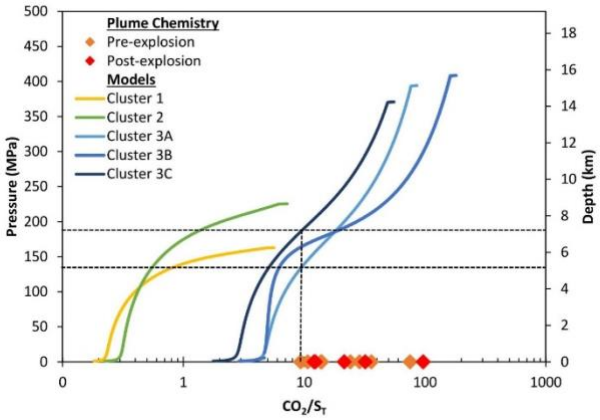

Figure 11 – Comparison of CO_2/S_T measured in the plume and CO_2/S_T modelled using Sulfur_X (Ding et al., 2023), based on our melt inclusion dataset as a function of pressure and depth suggests magmatic degassing at depths of 5.4-7.3 km. Cluster 1 represents the group of melt inclusions in the shallow depth zone at ~5 km. Starting H_2O, CO_2 and S concentrations are 4.20 wt.%, 79 ppm and 245 ppm respectively. Cluster 2 represents the group of inclusions clustered around ~9 km depth. Starting compositions are 5.20 wt.% H_2O, 245 ppm CO_2 and 567 ppm S. Clusters 3A and 3B represent the deepest plotting melt inclusions at ~22 km depth. Starting compositions are 4.46 wt.% H_2O, 3037 ppm CO_2 and 452 ppm S. In Cluster 3A, crystallisation is turned off during modelling. In Cluster 3B, crystallisation is turned on. Running the model with crystallisation off allows a single melt composition during decompression. Cluster 3C represents the deepest plotting olivine-hosted melt inclusion (which has the highest S concentration) at 21 km depth. Its starting compositions are 4.88 wt.% H_2O, 2506 ppm CO_2 and 620 ppm S.

Magmatic Volatile Budget

Quantification of pre-eruptive volatile budgets and atmospheric fluxes can contribute to the understanding of magma degassing and evolution, as well as help to constrain the baseline values of volcanic systems, which can provide insights into global carbon and sulphur cycles (e.g. Gerlach and Graeber, 1985; Fischer, 2008; Burton et al., 2013; Aiuppa et al., 2019). Such quantification is also critically important for volcano monitoring and defining the potential atmospheric, climatic, environmental, and health effects of volatile loading into the atmosphere (e.g. Devine et al., 1984; Graf et al., 1997; Robock, 2000; Scaillet et al., 2003; Hansell and Oppenheimer, 2004; Longo et al., 2005; Witt et al., 2008; Martin et al., 2009; Oppenheimer et al., 2011; Ge et al., 2016; Carn et al., 2017).

The SO_2 flux is of particular importance, as it is used to derive other volatile fluxes using species ratios during degassing (e.g. Edmonds et al., 2014). While SO_2 is readily measured by remote sensing techniques (Oppenheimer et al., 2011; Carn et al., 2016), the database of SO_2 fluxes is affected by spatial and temporal availability of ground-based measurements (Carn et al., 2017). However, global estimates of SO_2 fluxes from volcanoes in subduction zones, hotspots and rift-zones are roughly 21-23 Mt/year (Hilton et al.,2002; Shinohara et al., 2013; Carn et al., 2017). CO_2 is an important climate-warming greenhouse gas and is released from crustal storage through volcanoes (Burton et al., 2013). As of 2013, there had been 550-575 documented active volcanoes (Burton et al., 2013; Siebert et al., 2015), but quantification of CO_2 fluxes at fewer than 60 of these, from measurements of passive degassing through plumes and through diffuse degassing exists for only <60 volcanoes (Burton et al., 2013; Aiuppa et al., 2019). The scarcity in lack of direct measurements also relates to the rapid dilution of CO_2 in the atmosphere. Based on measurements from passive and diffuse degassing as well as from mid-ocean ridges and tectonic and hydrothermal degassing in inactive volcanic areas, the global CO_2 flux is estimated at 630 Mt/year (Burton et al., 2013).

To quantify the contribution of volatile flux at La Soufrière to global budgets, we use Equation 3, following the petrological method of Devine et al., (1984), whereby:

$$M_{dv} = (X_{MI} - X_{GG})V\rho\varepsilon \quad (3)$$

In the equation, M_{dv} is the mass of the dissolved volatile compound in the magma; X_{MI} is the concentration of the volatile element measured from melt inclusions (pre-eruptive volatile contents); X_{GG} is the concentration of the volatile element in the groundmass glass; V is the volume of erupted magma at 38.5 x 10^6 m^3 (Sparks et al., 2023); ρ is the density of the La Soufrière magma (2671 kg m^{-3}) calculated using the average of the whole rock compositions via DensityX (Iacovino and Till, 2019), and ε refers to the factor for converting the volatile elements into their respective compounds. The application of this method to crystal-free melt yields masses of 5.40±0.60 Mt H_2O, 0.37±0.04 Mt CO_2, 0.13±0.01 Mt SO_2, and 0.33±0.04 Mt HCl released during the explosive phase of the 2021 eruption. These values are deemed conservatively minimum values due to possibilities of unerupted volumes of magma not taken into account, due to the entrapment of already degassed magmas (Figure 10C), and due to sulphide saturation leading to S being lost to an immiscible Fe-S phase or to S-bearing minerals.

Since S was not measured in the groundmass glass, and because of the degassing trend of S in melt inclusions, the minimum S value of 59 ppm in the melt inclusions was used as a maximum concentration likely to be contained in the groundmass. We took the minimum groundmass Cl concentration of 846 ppm (Frey et al., 2023), and the average groundmass H_2O concentration of 0.2 wt.% (Phillips, 2023) and assumed that the groundmass is entirely CO_2 free. As F was not measured in

the groundmass, and do not have a degassing signature with differentiation, HF release from the magma cannot be estimated. Comparison of the mass of H_2O, CO_2, SO_2 and HCl dissolved in the melt (based on pre-eruptive volatile contents only) with the amount released during the explosive phase of the eruption indicates that a minimum of 96% magmatic H_2O, 100% CO_2, 100% SO_2, and 79% of HCl were released into the atmosphere.

In these calculations, SO_2 is assumed to be the only S species. However, S also exists as H_2S, with their relative proportions being dependent on factors such as temperature, pressure and redox conditions. In hydrous magmas, SO_2 exists primarily in oxidised conditions, at values above FMQ+1, whilst H_2S dominates in reduced conditions, below FMQ+1 (Carrol and Webster, 1994). The oxygen fugacity at La Soufrière exists around FMQ+2.08 (Bouvier et al., 2008), indicating S should exist mainly as SO_2, and that the SO_2 mass calculated in the magma is not greatly overestimated. Assuming SO_2 = total S, the mass of SO_2 dissolved in the magma that is estimated using the petrological method accounts for 26-50% of that released during the eruption (average 0.26-0.50 Mt over the 44 hours after the beginning of the eruption. This estimate uses total plume SO_2 emission rates based on satellite observations from TROPOMI (Esse et al., 2023).

However, our melt inclusion calculated values of SO_2 emissions (1.6±0.1 kt, calculated using a magma volume of $4.72\times10^5\pm3.16\times10^3$ m^3 from Sparks et al., 2023) match the total SO_2 mass measured via satellite (1.9±0.6 kt) over the first time window available from TROPOMI (UTC 1230 April 9th – 1420 April 9th 2021; Esse et al., 2023). This indicates that the first explosion (Vulcanian in nature) released all of the S dissolved in the melt. The second and third time windows (UTC 1700 April 9th – 1310 April 10th and 1800 April 10th – 0830 April 11th 2021) from TROPOMI show a significant increase in S emissions (Esse et al., 2023), which cannot be accounted for by melt inclusion-derived S. An excess S phase trapped at depth and released during the second and third time windows can explain this increase in S, as seen at various volcanoes (e.g. Scaillet et al., 2003; Sharma et al., 2004; Metcalfe et al., 2023). Moreover, this hypothesis is coherent with the fact that this apparent change in S content based on satellite observations coincide with a change in eruption style and explosivity from Vulcanian to sub-Plinian, highlighting the implication of a deeper gas phase input on eruptive style. We do not see any petrological evidence (e.g. solid or liquid S-phases) of this excessive degassing of S at La Soufrière, which is coherent with the immiscibility of the S liquid and the silicate magma due to density differences (Collins et al., 2012), which prevents this S-rich phase from being readily sampled, including by melt inclusions. This hypothesis suggests that our melt inclusion data are well representative of the first Vulcanian explosions, but cannot account for the rest of the eruption.

In a broader context of the Lesser Antilles arc, the 2021 La Soufrière SO_2 emissions are most comparable to those of Guadeloupe (1010 CE and 5680 BCE eruptions; Metcalfe et al., 2023) and Mt Peleé, Martinique 1902 (Scaillet et al., 2023) where released SO_2 ranged from 0.2-0.34 Mt, although their eruptions produced larger volumes of erupted material (Figure 12A). Our estimated SO_2 emissions are however far less than those produced by the 1995 eruption of Soufrière Hills Volcano, Montserrat (2.34 Mt; Scaillet et al., 2003) and the Roseau Tuff of Dominica (180 Mt), both of which have greater eruptive volumes at 4×10^8 and 3×10^{10} m^3 respectively (Scaillet et al., 2003). Overall, SO_2 emissions at La Soufrière and the wider volcanic arc generally have similar SO_2 outputs at similar erupted volumes compared to global arc volcanoes (Scaillet et al., 2003).

We also compare the calculated HCl emissions of (0.33 Mt) to those in the 1979 eruption of La Soufrière, as well as volcanoes in the Lesser Antilles and global arcs (Figure 12B). The 2021 eruption of La Soufrière saw the release of an order of a magnitude less HCl than the 1979 eruption (1.16 Mt; Devine et al., 19846), despite its similar erupted volume. Our values are, however, similar to those from eruptions from the Guadeloupe 1010 CE and 5680 BCE eruptions (0.3-0.4 Mt). Like that of SO_2, HCl emissions from the Roseau Tuff, Dominica (11.5 Mt) are much higher than those of other Lesser Antillean volcanoes, likely owing to larger volumes of magma erupted as can be seen in Figure 12. When we compare HCl emissions from La Soufriere and the Lesser Antilles with four other arc volcanoes (Agung – 1.53 Mt, Mt St Helens – 0.035 Mt, Krakatau – 3.75 Mt, Tambora – 216 Mt), Lesser Antilles volcanoes (except Dominica) fall outside of the global trend, producing comparable HCl at lower eruptive volumes than Agung and greater HCl emissions at lower eruptive volumes than Mt St Helens (Figure 12B).

In terms of global arc volcanoes, La Soufrière is not a great contributor of volatiles to the atmosphere, and together with Soufrière Hills Volcano, Montserrat, Roseau Tuff, Dominica, 1010 CE and 5680 BCE eruptions at of Guadeloupe and the 1902 eruption of Mt Peleé, Martinique, released volatiles on the order of minimum 5.5 Mt of SO_2 and HCl over the last 1000 years (based on the limited calculations available in the literature), which rivals the SO_2 release of the 181 AD eruption of Taupo volcano at 4.93 Mt for a similar erupted volume.

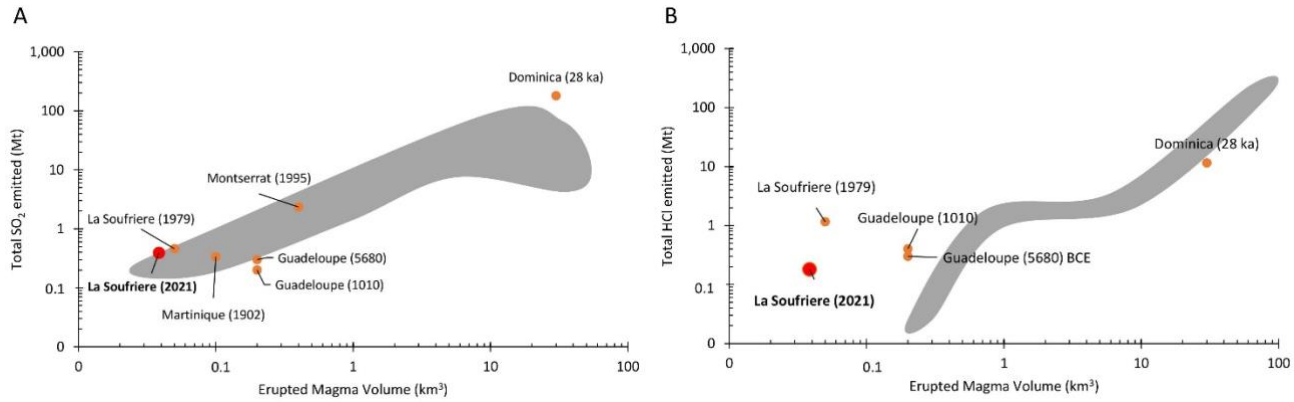

Figure 12: Volatile release vs magma volume at arc volcanoes globally. [A] Total SO_2 taking into account the gas phase for Lesser Antillean volcanoes. La Soufrière is generally comparable with other volcanoes in the arc, except for Dominica which has higher SO_2 emissions and greater erupted material. [B] HCl emissions from the melt phase for Lesser Antillean volcanoes. On both graphs, the grey shaded areas represent literature data on arc volcanoes outside of the Lesser Antilles. Data for SO_2 emissions from Scaillet et al., (2003) are presented for La Soufrière's 1979 eruption, Soufrière Hills Volcano, Montserrat, Roseau Tuff, Dominica and Mt Pelée, Martinique in the Lesser Antilles, and Agung, Bezymianny, Coseguina, El Chichon, Fuego, Huaynaputina, Katmai, Krakatau, Minoan, Mt St Helens, Pinatubo, Rabaul, Redoubt, Ruiz, Santa Maria, Tambora, Tarawera, Taupo and Unzen for global arcs. SO_2 data from Guadeloupe are from Metcalfe et al., (2023) for the 1010 CE and 5680 BCE eruptions. HCl literature data is from Devine et al., (1986) for Agung, Ht St Helens, Krakatau and Tambora volcanoes.

Conclusions

We have provided the full suite of volatile element compositions for the 2021 explosive products of La Soufrière (St Vincent), including the first measurements of total magmatic CO_2 in melt inclusions at this volcano. Concentrations of H_2O, S, Cl and F are generally comparable with previous measurements

and estimates at La Soufrière, and the first measurements of total CO_2 (where total CO_2 = CO_2 in the glass due to empty bubbles) range 3-661 ppm, with two measurements of 2506 and 3567 ppm. Based on the solubility relationship between H_2O and CO_2, melt inclusions re-equilibrated at depths of 2.4-8.9 km (mean 6.4 km) beneath La Soufrière. This depth range is similar to estimates obtained from geophysical data (deformation and seismicity) leading up to and during the course of the 2021 eruption, and also to petrologically-derived depths for reservoirs feeding pre-historic and the majority of historic eruptions.

Independent barometric estimates based on clinopyroxene-only compositions either yield a similar depth range (1.1-8.0 km) to the melt inclusions volatiles when the Wang (2021) model is employed, or greater depths (6.1-20.3 km) using Equation 30 of Putirka, (2008) that more closely match earlier studies of clinopyroxene from this eruption. However, significant depth uncertainties in clinopyroxene-only barometry (±~7km) mean that this technique cannot reliably differentiate between mid-crustal reservoirs.

We used several geothermometers to calculate magma temperature based on major element and H_2O contents, and show that temperatures of the 2021 eruptions are 970-1120 °C using the best fit thermometers, similar to published data for pre-historic and the 1979 eruptions. The release of H_2O, CO2, S and Cl were also quantified using the petrological method, which revealed that 5.43 Mt H_2O, 0.37 Mt CO_2, 0.13 Mt SO_2, and 0.33 Mt Cl were released into the atmosphere over April 9-22, 2021.

Author contributions

TAH, TEC, SM and HT co-developed the concept. PDC collected and provided samples. TAH prepared and analysed samples and processed and interpreted the data. SM guided data interpretation and TEC, HT and PDC contributed to data interpretation. FS contributed to Raman analysis and data processing. HT led PhD supervision and TC and SM co-supervised the PhD. TH drafted the manuscript and figures, and all authors contributed to the article.

Acknowledgements

This study was supported by a Government of Montserrat PhD scholarship awarded to TAH. We thank Cees-Jan de Hoog for assistance with ionprobe analysis, Jean Luc Deval for assistance with microprobe analysis and Claire Fonquernie for whole rock analysis. Raman and whole rock analyses were funded by the Volcanology team at Laboratoire Magmas et Volcans. We are grateful to David Neave and Margaret Hartley for discussions on melt inclusion reconstruction.

Data Availability

All data are available in Supplementary Materials.

References

Aiuppa, A., Bitetto, M., Francofonte, V., Velasquez, G., Parra, C. B., Giudice, G., Liuzzo, M., Moretti, R., Moussallam, Y., Peters, N., Tamburello, G., Valderrama, Oscar. A., & Curtis, A. (2017). A CO_2-gas precursor to the March 2015 Villarrica volcano eruption. Geochemistry, Geophysics, Geosystems, 18(6), 2120–2132. https://doi.org/10.1002/2017gc006892

Allison, C. M., Roggensack, K., & Clarke, A. B. (2022). MafiCH: a general model for H_2O–CO_2 solubility in mafic magmas. *Contributions to Mineralogy and Petrology*, *177*(3). https://doi.org/10.1007/s00410-022-01903-y

Anderson, A. T., & Brown, G. G. (1993). CO_2 contents and formation pressures of some Kilauean melt inclusions. *American Mineralogist*, *78*, 794–803.

Ariskin, A. A., & Barmina, G. S. (1996). An empirical model for the calculation of spinel-melt equilibria in mafic igneous systems at atmospheric pressure: 2. Fe-Ti oxides. *Contributions to Mineralogy and Petrology*, *134*(2-3), 251–263. https://doi.org/10.1007/s004100050482

Aspinall, W. P., Sigurdsson, H., & Shepherd, J. B. (1973). Eruption of Soufrière Volcano on St. Vincent Island, 1971-1972. *Science*, *181*(4095), 117–124. https://doi.org/10.1126/science.181.4095.117

Aster, E. M., Wallace, P. J., Moore, L. R., Watkins, J., Gazel, E., & Bodnar, R. J. (2016). Reconstructing CO_2 concentrations in basaltic melt inclusions using Raman analysis of vapor bubbles. *Journal of Volcanology and Geothermal Research*, *323*, 148–162. https://doi.org/10.1016/j.jvolgeores.2016.04.028

Bindeman, I. N., Kamenetsky, V. S., Palandri, J., & Vennemann, T. (2012). Hydrogen and oxygen isotope behaviors during variable degrees of upper mantle melting: Example from the basaltic glasses from Macquarie Island. *Chemical Geology*, *310–311*, 126–136. https://doi.org/10.1016/j.chemgeo.2012.03.031

Blundy, J., Cashman, K. V., Rust, A., & Witham, F. (2010). A case for CO_2-rich arc magmas. *Earth and Planetary Science Letters*, *290*(3-4), 289–301. https://doi.org/10.1016/j.epsl.2009.12.013

Bolikhovskaya, S. V., Vasil'eva, M. O., & Koptev-Dvornikov, E. V. (1995). Modelling of low-Ca pyroxene crystallisation in basic systems (New versions of geothermometers). *Geokhimia*, *12*, 1710–1727.

Borisov, A. A., & Shapkin, A. I. (1990). A new empirical equation rating Fe3+/Fe2+ in magmas to their composition, oxygen fugacity, and temperature. *Geochemistry International*, *27*, 111–116.

Bouvier, A. S., Métrich, N., & Deloule, E. (2008). Slab-Derived Fluids in the Magma Sources of St. Vincent (Lesser Antilles Arc): Volatile and Light Element Imprints. *Journal of Petrology*, *49*(8), 1427–1448. https://doi.org/10.1093/petrology/egn031

Bouvier, A.-S., Deloule, E., & Métrich, N. (2010). Fluid Inputs to Magma Sources of St. Vincent and Grenada (Lesser Antilles): New Insights from Trace Elements in Olivine-hosted Melt Inclusions. *Journal of Petrology*, *51*(8), 1597–1615. https://doi.org/10.1093/petrology/egq031

Briden, J. C., Rex, D. C., Faller, A. M., & Tomblin, J. F. (1979). K-Ar geochronology and palaeomagnetism of volcanic rocks in the Lesser Antilles island arc. *Philosophical Transactions of the Royal Society of London. Series A, Mathematical and Physical Sciences*, *291*(1383), 485–528. https://doi.org/10.1098/rsta.1979.0040

Brooker, R. A., Kohn, S. C., Holloway, J. R., McMillan, P. F., & Carroll, M. R. (1999). Solubility, speciation and dissolution mechanisms for CO2 in melts on the NaAlO2–sio2 join. *Geochimica et Cosmochimica Acta*, *63*(21), 3549–3565. https://doi.org/10.1016/s0016-7037(99)00196-9

Burton, M., Allard, P., MuréF., & La Spina, A. (2007). Magmatic Gas Composition Reveals the Source Depth of Slug-Driven Strombolian Explosive Activity. Science, 317(5835), 227–230. https://doi.org/10.1126/science.1141900

Burton, M., Hayer, C., Miller, C., & Christenson, B. (2021). Insights into the 9 December 2019 eruption of Whakaari/White Island from analysis of TROPOMI SO_2 imagery. *Science Advances*, *7*(25), eabg1218. https://doi.org/10.1126/sciadv.abg1218

Collins, S. J., Maclennan, J., Pyle, D. M., Barnes, S. J., & Upton, B. G. J. (2012). Two phases of sulphide saturation in Réunion magmas: Evidence from cumulates. *Earth and Planetary Science Letters*, *337–338*, 104–113. https://doi.org/10.1016/j.epsl.2012.05.027

Camejo-Harry, M., Pascal, K., Euillades, P., Grandin, R., Hamling, I., Euillades, L., Contreras-Arratia, R., Ryan, G. A., Latchman, J. L., Lynch, L., & Jo, M. (2023). Monitoring volcano deformation at La Soufrière, St Vincent during the 2020–21 eruption with insights into its magma plumbing system architecture. *Geological Society, London, Special Publications*, *539*(1), 41–62. https://doi.org/10.1144/sp539-2022-270

Caricchi, L., Sheldrake, T. E., & Blundy, J. (2018). Modulation of magmatic processes by CO_2 flushing. *Earth and Planetary Science Letters*, *491*, 160–171. https://doi.org/10.1016/j.epsl.2018.03.042

Carroll, M. R., & Webster, J. D. (1994). Chapter 7. SOLUBILITIES OF SULFUR, NOBLE GASES, NITROGEN, CHLORINE, AND FLUORINE IN MAGMAS. *De Gruyter EBooks*, 231–280. https://doi.org/10.1515/9781501509674-013

Carn, S. A., Clarisse, L., & Prata, A. J. (2016). Multi-decadal satellite measurements of global volcanic degassing. *Journal of Volcanology and Geothermal Research*, *311*, 99–134. https://doi.org/10.1016/j.jvolgeores.2016.01.002

Carn, S. A., Fioletov, V. E., McLinden, C. A., Li, C., & Krotkov, N. A. (2017). A decade of global volcanic SO2 emissions measured from space. *Scientific Reports*, *7*(1). https://doi.org/10.1038/srep44095

Cashman, K. V. and Mangan, M. T.. "Chapter 11b. PHYSICAL ASPECTS OF MAGMATIC DEGASSING II. Constraints on vesiculation processes from textural studies of eruptive products". *Volatiles in Magmas*, edited by Michael R. Carroll and John R. Holloway, Berlin, Boston: De Gruyter, 1994, pp. 447-478. https://doi.org/10.1515/9781501509674-018

Cassidy, M., Edmonds, M., Watt, S. F. L., Palmer, M. R., & Gernon, T. M. (2015). Origin of Basalts by Hybridization in Andesite-dominated Arcs. *Journal of Petrology*, *56*(2), 325–346. https://doi.org/10.1093/petrology/egv002

Cassidy, M., Manga, M., Cashman, K., & Bachmann, O. (2018). Controls on explosive-effusive volcanic eruption styles. *Nature Communications*, *9*(1), 2839. https://doi.org/10.1038/s41467-018-05293-3

Christeson, G. L., Mann, P., Escalona, A., & Aitken, T. J. (2008). Crustal structure of the Caribbean-northeastern South America arc-continent collision zone. *Journal of Geophysical Research: Solid Earth*, *113*(B8). https://doi.org/10.1029/2007jb005373

Christopher, T., Edmonds, M., Humphreys, M. C. S., & Herd, R. A. (2010). Volcanic gas emissions from Soufrière Hills Volcano, Montserrat 1995-2009, with implications for mafic magma supply and degassing. *Geophysical Research Letters*, *37*(19). https://doi.org/10.1029/2009gl041325

Cofano, A., Cigna, F., Santamaria Amato, L., Siciliani de Cumis, M., & Tapete, D. (2021). Exploiting Sentinel-5P TROPOMI and Ground Sensor Data for the Detection of Volcanic SO_2 Plumes and Activity in 2018–2021 at Stromboli, Italy. *Sensors*, *21*(21), 6991. https://doi.org/10.3390/s21216991

Cole, P. D., Barclay, J., Robertson, A., Mitchell, S., Davies, B. V., Constantinescu, R., Sparks, J., Aspinall, W., & Stinton, A. (2023). Explosive sequence of La Soufrière, St Vincent, April 2021: insights into drivers and consequences via eruptive products. Special Publication - Geological Society of

London/Geological Society, London, Special Publications, 539(1), 81–106. https://doi.org/10.1144/sp539-2022-292

Cole, P. D., Robertson, R. E. A., Fedele, L., & Scarpati, C. (2019). Explosive activity of the last 1000 years at La Soufrière, St Vincent, Lesser Antilles. *Journal of Volcanology and Geothermal Research*, *371*, 86–100. https://doi.org/10.1016/j.jvolgeores.2019.01.002

Cooper, G. F., Macpherson, C. G., Blundy, J. D., Maunder, B., Allen, R. W., Goes, S., Collier, J. S., Bie, L., Harmon, N., Hicks, S. P., Iveson, A. A., Prytulak, J., Rietbrock, A., Rychert, C. A., Davidson, J. P., Cooper, G. F., Macpherson, C. G., Blundy, J. D., Maunder, B., & Allen, R. W. (2020). Variable water input controls evolution of the Lesser Antilles volcanic arc. *Nature*, *582*(7813), 525–529. https://doi.org/10.1038/s41586-020-2407-5

d'Augustin, T., Balcone-Boissard, H., Boudon, G., Martel, C., Deloule, E., & Bürckel, P. (2020). Evidence for an Active, Transcrustal Magma System in the Last 60 ka and Eruptive Degassing Budget (H_2O, CO_2, S, F, Cl, Br): The Case of Dominica. *Geochemistry, Geophysics, Geosystems*, *21*(9). https://doi.org/10.1029/2020gc009050

Danyushevsky, L. V. (2001). The effect of small amounts of H_2O on crystallisation of mid-ocean ridge and backarc basin magmas. *Journal of Volcanology and Geothermal Research*, *110*(3-4), 265–280. https://doi.org/10.1016/s0377-0273(01)00213-x

Danyushevsky, L. V., & Plechov, P. (2011). Petrolog3: Integrated software for modeling crystallization processes. *Geochemistry, Geophysics, Geosystems*, *12*(7). https://doi.org/10.1029/2011gc003516

DeMets, C., Jansma, P. E., Mattioli, G. S., Dixon, T. H., Farina, F., Bilham, R., Calais, E., & Mann, P. (2000). GPS geodetic constraints on Caribbean-North America Plate Motion. *Geophysical Research Letters*, *27*(3), 437–440. https://doi.org/10.1029/1999gl005436

Devine, J. D., & Sigurdsson, H. (1983). The liquid composition and crystallization history of the 1979 Soufrière magma, St. Vincent, W.I. *Journal of Volcanology and Geothermal Research*, *16*(1-2), 1–31. https://doi.org/10.1016/0377-0273(83)90082-3

Devine, J. D., Sigurdsson, H., Davis, A. N., & Self, S. (1984). Estimates of sulfur and chlorine yield to the atmosphere from volcanic eruptions and potential climatic effects. *Journal of Geophysical Research: Solid Earth*, *89*(B7), 6309–6325. https://doi.org/10.1029/jb089ib07p06309

Ding, S., Plank, T., Wallace, P. J., & Rasmussen, D. J. (2023). Sulfur_X: A Model of Sulfur Degassing During Magma Ascent. *Geochemistry Geophysics Geosystems*, *24*(4). https://doi.org/10.1029/2022gc010552

Dohmen, R., Ter heege, J. H., Becker, H.-W., & Chakraborty, S. (2016). Fe-Mg interdiffusion in orthopyroxene. *American Mineralogist*, *101*(10), 2210–2221. https://doi.org/10.2138/am-2016-5815

Dualeh, E. W., Ebmeier, S. K., Wright, T. J., Poland, M. P., Grandin, R., Stinton, A. J., Camejo-Harry, M., Esse, B., & Burton, M. (2023). Rapid pre-explosion increase in dome extrusion rate at La Soufrière, St. Vincent quantified from synthetic aperture radar backscatter. *Earth and Planetary Science Letters*, *603*. https://doi.org/10.1016/j.epsl.2022.117980

Edmonds, M., & Wallace, P. J. (2017). Volatiles and Exsolved Vapor in Volcanic Systems. *Elements*, *13*(1), 29–34. https://doi.org/10.2113/gselements.13.1.29

Edmonds, M., & Woods, A. W. (2018). Exsolved volatiles in magma reservoirs. *Journal of Volcanology and Geothermal Research*, *368*, 13–30. https://doi.org/10.1016/j.jvolgeores.2018.10.018

Edmonds, M., Pyle, D., & Oppenheimer, C. (2001). A model for degassing at the Soufrière Hills Volcano, Montserrat, West Indies, based on geochemical data. *Earth and Planetary Science Letters*, *186*(2), 159–173. https://doi.org/10.1016/s0012-821x(01)00242-4

Esposito, R., Lamadrid, H. M., Redi, D., Steele-MacInnis, M., Bodnar, R. J., Manning, C. E., De Vivo, B., Cannatelli, C., & Lima, A. (2016). Detection of liquid H_2O in vapor bubbles in reheated melt inclusions: Implications for magmatic fluid composition and volatile budgets of magmas?. *The American Mineralogist*, *101*(7), 1691–1695. https://doi.org/10.2138/am-2016-5689

Esse, B., Burton, M., Hayer, C., Contreras-Arratia, R., Christopher, T., Joseph, E. P., Varnam, M., & Johnson, C. (2023). SO_2 emissions during the 2021 eruption of La Soufrière, St Vincent, revealed with back-trajectory analysis of TROPOMI imagery. *Geological Society London Special Publications*, *539*(1), 231–244. https://doi.org/10.1144/sp539-2022-77

Evain, M., Galve, A., Charvis, P., Laigle, M., Kopp, H., Bécel, A., Weinzierl, W., Hirn, A., Flueh, E. R., & Gallart, J. (2011). Structure of the Lesser Antilles subduction forearc and backstop from 3D seismic refraction tomography. *Tectonophysics*, *603*, 55–67. https://doi.org/10.1016/j.tecto.2011.09.021

Fedele, L., Cole, P. D., Scarpati, C., & Robertson, R. E. A. (2021). Petrological insights on the last 1000 years of explosive activity at La Soufrière volcano, St. Vincent (Lesser Antilles). *Lithos*, *392-393*, 106150. https://doi.org/10.1016/j.lithos.2021.106150

Feignon, J. G., Cluzel, N., Schiavi, F., Moune, S., Roche, O., Clavero, J., Schiano, P., & Auxerre, M. (2022). High CO_2 content in magmas of the explosive andesitic Enco eruption of Mocho-Choshuenco volcano (Chile). *Bulletin of Volcanology*, *84*(4). https://doi.org/10.1007/s00445-022-01550-y

Frey, H. M., Manon, M. R., Barclay, J., Davies, B. V., Walters, S. A., Cole, P. D., Christopher, T. E., & Joseph, E. P. (2023). Petrology of the explosive deposits from the April 2021 eruption of La Soufrière volcano, St Vincent: a time-series analysis of microlites. *Geological Society, London, Special Publications*, *539*(1), 201–230. https://doi.org/10.1144/sp539-2022-291

Frezzotti, M. L., Tecce, F., & Casagli, A. (2012). Raman spectroscopy for fluid inclusion analysis. *Journal of Geochemical Exploration*, *112*, 1–20. https://doi.org/10.1016/j.gexplo.2011.09.009

Gaetani, G. A., O'Leary, J. A., Shimizu, N., Bucholz, C. E., & Newville, M. (2012). Rapid reequilibration of H_2O and oxygen fugacity in olivine-hosted melt inclusions. *Geology*, *40*(10), 915–918. https://doi.org/10.1130/g32992.1

Gerlach, T. M., & Graeber, E. J. (1985). Volatile budget of Kilauea volcano. *Nature*, *313*(6000), 273–277. https://doi.org/10.1038/313273a0

Ghiorso, M. S., & Gualda, G. A. R. (2015). An H_2O–CO_2 mixed fluid saturation model compatible with rhyolite-MELTS. *Contributions to Mineralogy and Petrology*, *169*(6). https://doi.org/10.1007/s00410-015-1141-8

Giordano, D., & Dingwell, D. B. (2003). Non-Arrhenian multicomponent melt viscosity: a model. *Earth and Planetary Science Letters*, *208*(3-4), 337–349. https://doi.org/10.1016/s0012-821x(03)00042-6

Giordano, D., Russell, J. K., & Dingwell, D. B. (2008). Viscosity of magmatic liquids: A model. *Earth and Planetary Science Letters*, *271*(1-4), 123–134. https://doi.org/10.1016/j.epsl.2008.03.038

Graham, A. M., & Thirlwall, M. F. (1981). Petrology of the 1979 eruption of Soufrière volcano, St. Vincent, Lesser Antilles. *Contributions to Mineralogy and Petrology*, *76*(3), 336–342. https://doi.org/10.1007/bf00375460

Gurenko, A. A., Trumbull, R. B., Thomas, R., & Lindsay, J. M. (2005). A Melt Inclusion Record of Volatiles, Trace Elements and Li–B Isotope Variations in a Single Magma System from the Plat Pays Volcanic Complex, Dominica, Lesser Antilles. *Journal of Petrology*, *46*(12), 2495–2526. https://doi.org/10.1093/petrology/egi063

Hansell, A., & Oppenheimer, C. (2004). Health hazards from volcanic gases: A systematic literature review. *Archives of Environmental Health: An International Journal*, *59*(12), 628–639. https://doi.org/10.1080/00039890409602947

Hanyu, T., Yamamoto, J., Kimoto, K., Shimizu, K., & Ushikubo, T. (2020). Determination of total CO_2 in melt inclusions with shrinkage bubbles. *Chemical Geology*, *557*, 119855–119855. https://doi.org/10.1016/j.chemgeo.2020.119855

Hartley, M. E., Maclennan, J., Edmonds, M., & Thordarson, T. (2014). Reconstructing the deep CO_2 degassing behaviour of large basaltic fissure eruptions. *Earth and Planetary Science Letters*, *393*, 120–131. https://doi.org/10.1016/j.epsl.2014.02.031

Hauri, E., Wang, J., Dixon, J. E., King, P. L., Mandeville, C., & Newman, S. (2002). Sims analysis of volatiles in silicate glasses. *Chemical Geology*, *183*(1–4), 99–114. https://doi.org/10.1016/s0009-2541(01)00375-8

Heath, E., Macdonald, R., Belkin, H., Hawkesworth, C., & Sigurdsson, H. (1998). Magmagenesis at Soufrière Volcano, St Vincent, Lesser Antilles Arc. *Journal of Petrology*, *39*(10), 1721–1764. https://doi.org/10.1093/petroj/39.10.1721

Howe, T. A., Christopher, T. E., Moune, S., Tuffen, H., & Schiavi, F. (2025). Melt inclusion bubbles provide new insights into crystallisation depths and CO_2 systematics at Soufrière Hills Volcano, Montserrat. *Frontiers in Earth Science*, *12*. https://doi.org/10.3389/feart.2024.1509409

Humphreys, M. C. S., Edmonds, M., & Klöcking, M. S. (2016). The validity of plagioclase-melt geothermometry for degassing-driven magma crystallization. *The American Mineralogist*, *101*(4), 769–779. https://doi.org/10.2138/am-2016-5314

Iacono-Marziano, G., Morizet, Y., Le Trong, E., & Gaillard, F. (2012). New experimental data and semi-empirical parameterization of H_2O–CO_2 solubility in mafic melts. Geochimica et Cosmochimica Acta, 97, 1–23. https://doi.org/10.1016/j.gca.2012.08.035

Iacovino, K., & Till, C. B. (2018). DensityX: A program for calculating the densities of hydrous magmatic liquids from 427-1,627 °C and up to 30 kbar. *Volcanica*, *2*(1), 1–10. https://doi.org/10.30909/vol.02.01.0110

Iacovino, K., Matthews, S., Wieser, P. E., Moore, G., & Bégué, F. (2021). VESIcal Part I: An Open-Source Thermodynamic Model Engine for Mixed Volatile (H_2O-CO_2) Solubility in Silicate Melts. *Earth and Space Science*, *8*(11). https://doi.org/10.1029/2020ea001584

Jochum, K. P., Stoll, B., Herwig, K., Willbold, M., Hofmann, A. W., Amini, M., Aarburg, S., Abouchami, W., Hellebrand, E., Mocek, B., Raczek, I., Stracke, A., Alard, O., Bouman, C., Becker, S., Dücking, M., Brätz, H., Klemd, R., de Bruin, D., … Woodhead, J. D. (2006a). MPI-Ding reference

glasses for in situ microanalysis: New reference values for element concentrations and isotope ratios. *Geochemistry, Geophysics, Geosystems*, *7*(2). https://doi.org/10.1029/2005gc001060

Jochum, K. P., Stoll, B., Herwig, K., Willbold, M., Hofmann, A. W., Amini, M., Aarburg, S., Abouchami, W., Hellebrand, E., Mocek, B., Raczek, I., Stracke, A., Alard, O., Bouman, C., Becker, S., Dücking, M., Brätz, H., Klemd, R., de Bruin, D., … Woodhead, J. D. (2006b). MPI-Ding reference glasses for in situ microanalysis: New reference values for element concentrations and isotope ratios. *Geochemistry, Geophysics, Geosystems*, *7*(2). https://doi.org/10.1029/2005gc001060

Johnson, M., Anderson Jr., A. & Rutherford, M. (1994). Chapter 8. PRE-ERUPTIVE VOLÀTILE CONTENTS OF MAGMAS. In M. Carroll & J. Holloway (Ed.), *Volatiles in Magmas* (pp. 281-330). Berlin, Boston: De Gruyter. https://doi.org/10.1515/9781501509674-014

Joseph, E. P., Camejo-Harry, M., Christopher, T., Contreras-Arratia, R., Edwards, S., Graham, O., Johnson, M., Juman, A., Latchman, J. L., Lynch, L., Miller, V. L., Papadopoulos, I., Pascal, K., Robertson, R., Ryan, G. A., Stinton, A., Grandin, R., Hamling, I., Jo, M. J., & Barclay, J. (2022). Responding to eruptive transitions during the 2020–2021 eruption of La Soufrière volcano, St. Vincent. *Nature Communications*, *13*(1), 4129. https://doi.org/10.1038/s41467-022-31901-4

Jugo, P. J., Luth, R. W., & Richards, J. P. (2005). An experimental study of the sulfur content in basaltic melts saturated with immiscible sulfide or sulfate liquids at 1300 c and 1{Middle Dot}0 GPA. *Journal of Petrology*, *46*(4), 783–798. https://doi.org/10.1093/petrology/egh097

Jugo, P. J. (2009). Sulfur content at sulfide saturation in oxidized magmas. *Geology*, *37*(5), 415–418. https://doi.org/10.1130/g25527a.1

Kent, A. J. R. (2008). Melt Inclusions in Basaltic and Related Volcanic Rocks. *Reviews in Mineralogy and Geochemistry*, *69*(1), 273–331. https://doi.org/10.2138/rmg.2008.69.8

Kilgour, G., Moune, S., Christenson, B., & Pasqua, F. D. (2021). Insights into the 1976–2000 eruption episode of Whakaari/White Island, New Zealand: An eruption fuelled by repeated mafic recharge. *Bulletin of Volcanology*, *83*(6). https://doi.org/10.1007/s00445-021-01460-5

Kopp, H., Weinzierl, W., Bécel, A., Charvis, P., Evain, M., Flueh, E. R., Gailler, A., Galve, A., Hirn, A., Kandilarov, A., Klaeschen, D., Laigle, M., Papenberg, C., Planert, L., & Roux, E. (2011). Deep structure of the central Lesser Antilles Island Arc: Relevance for the formation of continental crust. *Earth and Planetary Science Letters*, *304*(1-2), 121–134. https://doi.org/10.1016/j.epsl.2011.01.024

Lamadrid, H. M., Moore, L. A., Moncada, D., Rimstidt, J. D., Burruss, R. C., & Bodnar, R. J. (2017). Reassessment of the Raman CO_2 densimeter. *Chemical Geology*, *450*, 210–222. https://doi.org/10.1016/j.chemgeo.2016.12.034

Latchman, J. L., & Aspinall, W. (2023). La Soufrière volcano, St Vincent, eruption 2020–21: assessing unrest and eruptive states from limited volcano-seismic data. *Geological Society, London, Special Publications*, *539*(1). https://doi.org/10.1144/sp539-2022-223

Le Bas, M.J., Maitre, R.W.L., Streckeisen, A. and Zanettin, B. (1986). A Chemical Classification of Volcanic Rocks Based on the Total Alkali-Silica Diagram. Journal of Petrology, 27(3), pp.745–750. doi:https://doi.org/10.1093/petrology/27.3.745.

Le Friant, A., Boudon, G., Arnulf, A., & Robertson, R. E. A. (2009). Debris avalanche deposits offshore St. Vincent (West Indies): Impact of flank-collapse events on the morphological evolution of the island. *Journal of Volcanology and Geothermal Research*, *179*(1-2), 1–10. https://doi.org/10.1016/j.jvolgeores.2008.09.022

Le Gall, N., & Pichavant, M. (2016). Homogeneous bubble nucleation in H 2 O- and H 2 O-CO 2 -bearing basaltic melts: Results of high temperature decompression experiments. *Journal of Volcanology and Geothermal Research*, *327*, 604–621.

Lindsay, J. M., Robertson, R. E. A., Shepherd, J. B., & Ali, S. (Eds.). (2005). *Volcanic Hazard Atlas of the Lesser Antilles*. Seismic Research Unit, The University of the West Indies.

Lowenstern, J. (1995). Applications of silicate melt inclusions to the study of magmatic volatiles. In J. F. H. Thompson (Ed.), *Magmas, Fluids and Ore Deposits* (pp. 71–99). Mineralogical Association of Canada Short Course Volume.

Macdonald, R., Hawkesworth, C. J., & Heath, E. (2000). The Lesser Antilles volcanic chain: a study in arc magmatism. *Earth-Science Reviews*, *49*(1-4), 1–76. https://doi.org/10.1016/s0012-8252(99)00069-0

Maclennan, J. (2017). Bubble formation and decrepitation control theco2content of olivine-hosted melt inclusions. *Geochemistry, Geophysics, Geosystems*, *18*(2), 597–616. https://doi.org/10.1002/2016gc006633

Mann, C. P., Wallace, P. J., & Stix, J. (2013). Phenocryst-hosted melt inclusions record stalling of magma during ascent in the conduit and upper magma reservoir prior to vulcanian explosions, Soufrière Hills volcano, Montserrat, West Indies. *Bulletin of Volcanology*, *75*(2). https://doi.org/10.1007/s00445-013-0687-4

Marianelli, P., Sbrana, A., Métrich, N., & Cecchetti, A. (2005). The deep feeding system of Vesuvius involved in recent violent strombolian eruptions. *Geophysical Research Letters*, *32*(2). https://doi.org/10.1029/2004gl021667

Melekhova, E., Blundy, J., Robertson, R., & Humphreys, M. C. S. (2015). Experimental Evidence for Polybaric Differentiation of Primitive Arc Basalt beneath St. Vincent, Lesser Antilles. *Journal of Petrology*, *56*(1), 161–192. https://doi.org/10.1093/petrology/egu074

Melekhova, E., Schlaphorst, D., Blundy, J., Kendall, J.-M., Connolly, C., McCarthy, A., & Arculus, R. (2019). Lateral variation in crustal structure along the Lesser Antilles arc from petrology of crustal xenoliths and seismic receiver functions. *Earth and Planetary Science Letters*, *516*, 12–24. https://doi.org/10.1016/j.epsl.2019.03.030

Metcalfe, A., Moune, S., Moretti, R., Komorowski, J., & Aubry, T. J. (2023). Volatile emissions from past eruptions at La Soufrière de Guadeloupe (Lesser Antilles): insights into degassing processes and atmospheric impacts. *Frontiers in Earth Science*, *11*. https://doi.org/10.3389/feart.2023.1143325

Metrich, N., & Wallace, P. J. (2008). Volatile Abundances in Basaltic Magmas and Their Degassing Paths Tracked by Melt Inclusions. *Reviews in Mineralogy and Geochemistry*, *69*(1), 363–402. https://doi.org/10.2138/rmg.2008.69.10

Moldover, M. R. (1974). Visual observation of the critical temperature and density: CO_2 and C_2H_4. *Journal of Chemical Physics Online/˜the œJournal of Chemical Physics/Journal of Chemical Physics*, *61*(5), 1766–1778. https://doi.org/10.1063/1.1682173

Moore, L. R., & Bodnar, R. J. (2019). A pedagogical approach to estimating the CO_2 budget of magmas. *Journal of the Geological Society*, *176*(2), 398–407. https://doi.org/10.1144/jgs2018-094

Moore, L., Gazel, E., Tuohy, R. M., Hodder, S., Esposito, R., Steele-MacInnis, M., Hauri, E. H., Wallace, P. K., Plank, T., & Bodnar, R. J. (2015). Bubbles matter: An assessment of the contribution of vapor bubbles to melt inclusion volatile budgets. *American Mineralogist*, *100*(4), 806–823. https://doi.org/10.2138/am-2015-5036

Müller, T., Dohmen, R., Becker, H. W., ter Heege, J., & Chakraborty, S. (2013). Fe–Mg interdiffusion rates in clinopyroxene: experimental data and implications for Fe–Mg exchange geothermometers. *Contributions to Mineralogy and Petrology*, *166*(6), 1563–1576. https://doi.org/10.1007/s00410-013-0941-y

Neave, D. A., Hartley, M. E., Maclennan, J., Edmonds, M., & Thordarson, T. (2017). Volatile and light lithophile elements in high-anorthite plagioclase-hosted melt inclusions from Iceland. *Geochimica et Cosmochimica Acta*, *205*, 100–118. https://doi.org/10.1016/j.gca.2017.02.009

Newman, S., and Lowenstern, J. B. (2002). VolatileCalc: a silicate melt–H_2O–CO_2 solution model written in Visual Basic for excel. *Computers & Geosciences*, *28*(5), 597–604. https://doi.org/10.1016/s0098-3004(01)00081-4

Newman, S., Epstein, S., & Stolper, E. (1988). Water, carbon dioxide, and hydrogen isotopes in glasses from the ca. 1340 A.D. eruption of the Mono Craters, California: Constraints on degassing phenomena and initial volatile content. *Journal of Volcanology and Geothermal Research*, *35*(1–2), 75–96. https://doi.org/10.1016/0377-0273(88)90007-8

Nielsen, R. L. (2011). The effects of re-homogenization on plagioclase hosted melt inclusions. *Geochemistry, Geophysics, Geosystems*, *12*(10), n/a-n/a. https://doi.org/10.1029/2011gc003822

O'Neill, H. St. C. (2021). The thermodynamic controls on sulfide saturation in silicate melts with application to ocean floor basalts. *Geophysical Monograph Series*, 177–213. https://doi.org/10.1002/9781119473206.ch10

Oppenheimer, C., Scaillet, B., & Martin, R. S. (2011). Sulfur degassing from volcanoes: Source conditions, surveillance, plume chemistry and earth system impacts. *Reviews in Mineralogy and Geochemistry*, *73*(1), 363–421. https://doi.org/10.2138/rmg.2011.73.13

Phillips, K. (2022). *Insights into Conduit Dynamics and Eruptive Behaviour During the April 2021 La Soufrière, St. Vincent Explosive Eruption* [MSc Thesis].

Pichavant, M., Mysen, B. O., & Macdonald, R. (2002). Source and H_2O content of high-MgO magmas in island arc settings: an experimental study of a primitive calc-alkaline basalt from St. Vincent, lesser antilles arc. *Geochimica et Cosmochimica Acta*, *66*(12), 2193–2209. https://doi.org/10.1016/s0016-7037(01)00891-2

Putirka, K. D. (2008). Thermometers and Barometers for Volcanic Systems. *Reviews in Mineralogy and Geochemistry*, *69*(1), 61–120. https://doi.org/10.2138/rmg.2008.69.3

Queißer, M., Burton, M. G., Theys, N., Pardini, F., Salerno, G., Caltabiano, T., Varnam, M., Esse, B., & Kazahaya, R. (2019). TROPOMI enables high resolution SO_2 flux observations from Mt. Etna, Italy, and beyond. *Scientific Reports*, *9*(1). https://doi.org/10.1038/s41598-018-37807-w

Rasmussen, D. J., Plank, T. A., Roman, D. C., & Zimmer, M. M. (2022). Magmatic water content controls the pre-eruptive depth of arc magmas. *Science*, *375*(6585), 1169–1172. https://doi.org/10.1126/science.abm5174

Rasmussen, D. J., Plank, T. A., Wallace, P. J., Newcombe, M. E., & Lowenstern, J. B. (2020). Vapor-bubble growth in olivine-hosted melt inclusions. *American Mineralogist*, *105*(12), 1898–1919. https://doi.org/10.2138/am-2020-7377

Robertson, A., Barclay, J., Joseph, E. P., & Sparks, J. (2023). An overview of the eruption of La Soufrière Volcano, St. Vincent 2020 to 2021. *Geological Society, London, Special Publications*, *539*(1). https://doi.org/10.1144/sp539-2023-95

Roedder, E. (1979). Origin and significance of magmatic inclusions. *Bulletin de Minéralogie*, *102*(5), 487–510. https://doi.org/10.3406/bulmi.1979.7299

Scaillet, B., Luhr, J. F., & Carroll, M. R. (2024). Petrological and Volcanological Constraints on Volcanic Sulfur Emissions to the Atmosphere. In A. Robock & C. Oppenheimer (Eds.), *Volcanism and the Earth's Atmosphere, Volume 139* (pp. 11–40). American Geophysical Union.

Scaillet, B., Luhr, J. F., & Carroll, M. R. (2024). Petrological and Volcanological Constraints on Volcanic Sulfur Emissions to the Atmosphere. In A. Robock & C. Oppenheimer (Eds.), *Volcanism and the Earth's Atmosphere, Volume 139* (pp. 11–40). American Geophysical Union.

Schiavi, F., Bolfan-Casanova, N., Buso, R., Laumonier, M., Laporte, D., Medjoubi, K., Venugopal, S., Gómez-Ulla, A., Cluzel, N., & Hardiagon, M. (2020). Quantifying magmatic volatiles by Raman microtomography of glass inclusion-hosted bubbles. *Geochemical Perspectives Letters*, *16*, 17–24. https://doi.org/10.7185/geochemlet.2038

Schipper, C. I., White, J. D. L., Houghton, B. F., Shimizu, N., & Stewart, R. B. (2010). Explosive submarine eruptions driven by volatile-coupled degassing at Lō`ihi Seamount, Hawai`i. *Earth and Planetary Science Letters*, *295*(3-4), 497–510. https://doi.org/10.1016/j.epsl.2010.04.031

Sharma, K., Blake, S., Self, S., & Krueger, A. J. (2004). SO_2emissions from basaltic eruptions, and the excess sulfur issue. *Geophysical Research Letters*, *31*(13). https://doi.org/10.1029/2004gl019688

Shepherd, J. B., Aspinall, W. P., Rowley, K. C., Pereira, J., Sigurdsson, H., Fiske, R. S., & Tomblin, J. F. (1979). The eruption of Soufrière volcano, St Vincent April–June 1979. *Nature*, *282*(5734), 24–28. https://doi.org/10.1038/282024a0

Shinohara, H. (2008). Excess degassing from volcanoes and its role on eruptive and intrusive activity. *Reviews of Geophysics*, *46*(4). https://doi.org/10.1029/2007rg000244

Shishkina, T. A., Botcharnikov, R. E., Holtz, F., Almeev, R. R., & Portnyagin, M. V. (2010). Solubility of H2O- and CO2-bearing fluids in tholeiitic basalts at pressures up to 500mpa. *Chemical Geology*, *277*(1–2), 115–125. https://doi.org/10.1016/j.chemgeo.2010.07.014

Siebert, L., Cottrell, E., Venzke, E., & Andrews, B. (2015). Earth's volcanoes and their eruptions: An overview. *The Encyclopedia of Volcanoes*, 239–255. https://doi.org/10.1016/b978-0-12-385938-9.00012-2

Sisson, T. W., & Grove, T. L. (1993). Temperatures and H2O contents of low-MGO high-alumina basalts. *Contributions to Mineralogy and Petrology*, *113*(2), 167–184. https://doi.org/10.1007/bf00283226

Smythe, D. J., Wood, B. J., & Kiseeva, E. S. (2017). The S content of silicate melts at sulfide saturation: New experiments and a model incorporating the effects of sulfide composition. *American Mineralogist*, *102*(4), 795–803. https://doi.org/10.2138/am-2017-5800ccby

Sobolev, A. V., Asafov, E. V., Gurenko, A. A., Arndt, N. T., Batanova, V. G., Portnyagin, M. V., Garbe-Schönberg, D., & Krasheninnikov, S. P. (2016). Komatiites reveal a hydrous archaean deep-mantle reservoir. *Nature*, *531*(7596), 628–632. https://doi.org/10.1038/nature17152

Sparks, J., Aspinall, W. P., Barclay, J., Renfrew, I. A., Contreras-Arratia, R., & Stewart, R. (2023). Analysis of magma flux and eruption intensity during the 2021 explosive activity at the Soufrière of St Vincent, West Indies. *Geological Society, London, Special Publications*, *539*(1), 63–79. https://doi.org/10.1144/sp539-2022-286

Spilliaert, N., Allard, P., Métrich, N., & Sobolev, A. V. (2006a). Melt inclusion record of the conditions of ascent, degassing, and extrusion of volatile-rich alkali basalt during the powerful 2002 flank eruption of Mount Etna (Italy). *Journal of Geophysical Research*, *111*(B4). https://doi.org/10.1029/2005jb003934

Spilliaert, N., Metrich, N., & Allard, P. (2006b). S–Cl–F degassing pattern of water-rich alkali basalt: Modelling and relationship with eruption styles on Mount Etna volcano. *Earth and Planetary Science Letters*, *248*(3-4), 772–786. https://doi.org/10.1016/j.epsl.2006.06.031

Steele-Macinnis, M., Esposito, R., & Bodnar, R. J. (2011). Thermodynamic Model for the Effect of Post-entrapment Crystallization on the H_2O-CO_2 Systematics of Vapor-saturated, Silicate Melt Inclusions. *Journal of Petrology*, *52*(12), 2461–2482. https://doi.org/10.1093/petrology/egr052

Stinton, A. J. (2023). Growth and evolution of the lava dome and coulée during the 2020–21 eruption of La Soufrière, St Vincent. *Geological Society, London, Special Publications*, *539*(1), 25–39. https://doi.org/10.1144/sp539-2022-304

Sugawara, T. (2000). Empirical relationships between temperature, pressure, and MgO content in olivine and pyroxene saturated liquid. *Journal of Geophysical Research: Solid Earth*, *105*(B4), 8457–8472. https://doi.org/10.1029/2000jb900010

Symonds, R. B., Gerlach, T. M., & Reed, M. H. (2001). Magmatic gas scrubbing: implications for volcano monitoring. *Journal of Volcanology and Geothermal Research*, *108*(1-4), 303–341. https://doi.org/10.1016/s0377-0273(00)00292-4

Theys, N., Hedelt, P., De Smedt, I., Lerot, C., Yu, H., Vlietinck, J., Pedergnana, M., Arellano, S., Galle, B., Fernandez, D., Carlito, C. J. M., Barrington, C., Taisne, B., Delgado-Granados, H., Loyola, D., & Van Roozendael, M. (2019). Global monitoring of volcanic SO_2 degassing with unprecedented resolution from TROPOMI onboard Sentinel-5 Precursor. *Scientific Reports*, *9*(1). https://doi.org/10.1038/s41598-019-39279-y

Toplis, M. J. (2004). The thermodynamics of iron and magnesium partitioning between olivine and liquid: criteria for assessing and predicting equilibrium in natural and experimental systems. *Contributions to Mineralogy and Petrology*, *149*(1), 22–39. https://doi.org/10.1007/s00410-004-0629-4

Tucker, J. M., Hauri, E. H., Pietruszka, A. J., Garcia, M. O., Marske, J. P., & Trusdell, F. A. (2019). A high carbon content of the Hawaiian mantle from olivine-hosted melt inclusions. *Geochimica et Cosmochimica Acta*, *254*, 156–172. https://doi.org/10.1016/j.gca.2019.04.001

Venugopal, S., Schiavi, F., Moune, S., Bolfan-Casanova, N., Druitt, T., & Williams-Jones, G. (2020). Melt inclusion vapour bubbles: the hidden reservoir for major and volatile elements. *Scientific Reports*, *10*(1). https://doi.org/10.1038/s41598-020-65226-3

Wadge, G. (1984). Comparison of volcanic production rates and subduction rates in the Lesser Antilles and Central America. *Geology*, *12*(9), 555–558. https://doi.org/10.1130/0091-7613(1984)12%3C555:covpra%3E2.0.co;2

Wallace, P. J. (2001). Volcanic SO_2 emissions and the abundance and distribution of exsolved gas in magma bodies. *Journal of Volcanology and Geothermal Research*, *108*(1-4), 85–106.

Wallace, P. J. (2003). From mantle to atmosphere: magma degassing, explosive eruptions, and volcanic volatile budgets. *Melt Inclusions in Volcanic Systems - Methods, Applications and Problems*, *5*, 105–127. https://doi.org/10.1016/s1871-644x(03)80026-8

Wallace, P. J. (2005). Volatiles in subduction zone magmas: concentrations and fluxes based on melt inclusion and volcanic gas data. *Journal of Volcanology and Geothermal Research*, *140*(1-3), 217–240. https://doi.org/10.1016/j.jvolgeores.2004.07.023

Wallace, P. K., Meffre, S., & Cervantes, P. (2015). Melt inclusion CO_2 contents, pressures of olivine crystallization, and the problem of shrinkage bubbles. *American Mineralogist*, *100*(4), 787–794. https://doi.org/10.2138/am-2015-5029

Wang, X., Hou, T., Wang, M., Zhang, C., Zhang, Z., Pan, R., Marxer, F., & Zhang, H. (2021). A new clinopyroxene thermobarometer for mafic to intermediate magmatic systems. *European Journal of Mineralogy*, *33*(5), 621–637. https://doi.org/10.5194/ejm-33-621-2021

Waters, L. E., & Lange, R. A. (2015). An updated calibration of the plagioclase-liquid hygrometer-thermometer applicable to basalts through rhyolites. *American Mineralogist*, *100*(10), 2172–2184.

Weber, G., Blundy, J., Barclay, J., Pyle, D. M., Cole, P., Frey, H., Manon, M., Davies, B. V., & Cashman, K. (2023). Petrology of the 2020–21 effusive to explosive eruption of La Soufrière Volcano, St Vincent: insights into plumbing system architecture and magma assembly mechanism. *Geological Society, London, Special Publications*, *539*(1), 171–200. https://doi.org/10.1144/sp539-2022-177

Westrich, H. R., & Gerlach, T. M. (1992). Magmatic gas source for the stratospheric SO_2 cloud from the June 15,1991, eruption of Mount Pinatubo. *Geology*, *20*(10), 867.

Wieser, P., Kent, A. J. R., & Till, C. B. (2023). Barometers Behaving Badly II: a Critical Evaluation of Cpx-Only and Cpx-Liq Thermobarometry in Variably-Hydrous Arc Magmas. *Journal of Petrology*, *64*(8). https://doi.org/10.1093/petrology/egad050

Witham, F. (2010). Conduit convection, magma mixing, and melt inclusion trends at persistently degassing volcanoes. *Earth and Planetary Science Letters*, *301*(1-2), 345–352. https://doi.org/10.1016/j.epsl.2010.11.017

Witham, F., Blundy, J. D., Kohn, S. C., Lesne, P., Dixon, J., Churakov, S. V., & Botcharnikov, R. E. (2012). SolEx: A model for mixed COHSCl-volatile solubilities and exsolved gas compositions in basalt. *Computers & Geosciences*, *45*, 87–97. https://doi.org/10.1016/j.cageo.2011.09.021

1755

Tables

1760

Sample Specifications				Characteristics of Unit
Unit	**Duration/Time (UTC)**	**Sample**	**Distance to vent (km)**	
Unit 1	1241 April 9th – 0724 April 10th	LS21-99a	2.0	• Basal deposit • Plume heights of 13 – 16 km • 3.3 x 10^{10} kg of material ejected at maximum rate of 830 m^3 s^{-1} • Formation of 2021 crater
		LS21-97	6.2	
		LS21-76	1.3	
Unit 2	0935 – 1620 10th April	LS21-89	1.6	• Plume heights 13 – 16 km • 3.1 x 10^{10} kg of material ejected at maximum rate of ~400 m^3 s^{-1} • Ash rich with 7 lapilli layers
		LS21-98	6.2	
Unit 3	1830 – 2120 10th April	LS21-83	1.6	• Plume heights up to 16 km • First occurrence of PDC activity • Magma ejection rate of 200 – 300 m^3 s^{-1}
		LS21-87	1.6	
Unit 5	0051 – 0755 11th April	LS21-96	4.6	• Final scoria bearing unit • Plume heights up to 16 km • Magma discharge rate – 100 – 200 m^3 s^{-1}

Table 1: Sample details including time of formation of individual units deposited, along with brief characteristics. Compiled from Cole et al., (2023); Esse et al., (2023); Sparks et al., (2023).

	H_2O (wt.%)	**CO_2 (ppm)**	**S (ppm)**	**ΔFMQ +**	**Temp (°C)**	**Crystallisation**
Cluster 1	4.20	79	245	2.08	1050	no

Cluster 2	5.20	245	567	2.08	1110	no
Cluster 3A	4.46	3037	452	2.08	1096	no
Cluster 3B	4.46	3037	452	2.08	1096	yes
Cluster 3C	4.88	2506	620	2.08	1120	no

Table 2 – Input parameters for the modelling of CO_2/S_T using Sulfur_X (Ding et al., 2023). The three main groups of melt inclusions within our dataset are represented, and an average composition is used for Clusters 1-3B. 3C represents an olivine-hosted melt inclusion with the highest S from Cluster 3. Input parameters are as follows: In all models, COH saturation model of Iacono-Mariziano et al., (2012) and S speciation model of O'Neill and Mavrogenes, (2002) was used and fO_2 is buffered at FMQ+2.08. The total number of steps of pressure from initial pressure as calculated using Iacono-Mariziano et al., (2012) to 1 bar equals 600. All models are run with degassing and sulphide precipitation turned off. In models where crystallisation is off, the melt composition remains the same during decompression and is an averaged composition for Hawaiian magma. Where crystallisation is on, the melt composition evolves as a function of melt fraction and assumes a composition similar to Fuego volcano. Models 1, 2 and 3C were not able to resolve coherent degassing paths with crystallisation on.

	Mass in melt phase (Mt)	**Mass released from melt (Mt)**	**% released from melt**
H_2O	5.60±0.62	5.40±0.60	96
CO_2	0.37±0.04	0.37±0.04	100
SO_2	0.13±0.01	0.13±0.01	100
HCl	0.42±0.05	0.33±0.04	79
HF	0.85±0.09	-	-

Table 3 - The minimum mass of volatiles dissolved in and released from La Soufriere melt during the April 2021 explosive phase of eruption. Fluorine was not measured in the groundmass glass and does not have a degassing signature, thus, mass released could not be estimated.